

1 **Augmentation ~~and Use~~ of WRF-Hydro to Simulate Overland Flow-**
2 **and Streamflow-Generated Debris Flow ~~Hazards~~Susceptibility in**
3 **Burn Scars**

4
5 **Chuxuan Li¹, Alexander L. Handwerger^{2,3}, Jiali Wang⁴, Wei Yu^{5,6}, Xiang Li⁷, Noah J.**
6 **Finnegan⁸, Yingying Xie^{9,10}, Giuseppe Buscarnera⁷, and Daniel E. Horton¹**

7 ¹ Department of Earth and Planetary Sciences, Northwestern University, Evanston, IL, 60208, USA

8 ² Joint Institute for Regional Earth System Science and Engineering, University of California, Los Angeles,
9 CA, 90095, USA

10 ³ Jet Propulsion Laboratory, California Institute of Technology, Pasadena, CA, 91109, USA

11 ⁴ Environmental Science Division, Argonne National Laboratory, Lemont, IL, 60439, USA

12 ⁵ Cooperative Institute for Research in Environmental Sciences, University of Colorado Boulder, CO,
13 80309, USA

14 ⁶ NOAA/Global Systems Laboratory, 325 Broadway Boulder, Denver, CO, 80305-3328, USA

15 ⁷ Department of Civil and Environmental Engineering, Northwestern University, Evanston, IL, 60208, USA

16 ~~⁸University of California Santa Cruz,~~⁸ Department of Earth and Planetary Sciences, University of California
17 Santa Cruz, Santa Cruz, CA, 95064, USA

18 ⁹ Program in Environmental Sciences, Northwestern University, 2145 Sheridan Road, Evanston, IL, 60208,
19 USA

20 ¹⁰ Department of Biological Sciences, Purdue University, 915 W State St, West Lafayette, IN 47907, USA

21
22 *Correspondence to:* Chuxuan Li (chuxuanli2020@u.northwestern.edu)
23
24
25
26
27
28
29
30

Style Definition: Heading 3

Style Definition: Comment Text

Formatted: Superscript

31

32 **Abstract**

33 In steep wildfire-burned terrains, intense rainfall can produce large volumes of runoff that can
 34 trigger highly destructive debris flows. ~~The~~However, the ability to accurately characterize and
 35 forecast debris-flow ~~hazards~~susceptibility in burned terrains, ~~however, using physics-based tools~~
 36 remains limited. Here, we augment the Weather Research and Forecasting Hydrological modeling
 37 system (WRF-Hydro) to simulate both overland and channelized flows and assess postfire debris-
 38 flow ~~hazards~~susceptibility over a regional domain. We perform hindcast simulations using high-
 39 resolution weather radar-derived precipitation and reanalysis data to drive non-burned baseline
 40 and burn scar sensitivity experiments. Our simulations focus on January 2021 when an
 41 atmospheric river triggered numerous debris flows within a wildfire burn scar in Big Sur – one of
 42 which destroyed California’s famous Highway 1. Compared to the baseline, our burn scar
 43 simulation yields dramatic increases in total and peak discharge, and shorter lags between rainfall
 44 onset and peak discharge. ~~At Rat Creek, where Highway 1 was destroyed, discharge volume~~
 45 ~~increases eight fold and peak discharge triples relative to the baseline., consistent with streamflow~~
 46 ~~observations at nearby U.S. Geological Survey (USGS) streamflow gage sites. For all the 404~~
 47 ~~catchments within located in the simulated burn scar, we find that the area, median catchment-area~~
 48 ~~normalized discharge volume increases nine-fold after incorporating burn scar characteristics,~~
 49 ~~while the 95th percentile volume increases 13-fold. compared to the baseline.~~ Catchments with
 50 anomalously high ~~hazard levels~~catchment-area normalized discharge volumes correspond well
 51 with post-event field-based and remotely-sensed debris flow observations. ~~Our results demonstrate~~
 52 ~~that~~We suggest that our regional post-fire debris flow susceptibility analysis demonstrates WRF-
 53 Hydro ~~provides as~~ a compelling new physics-based tool whose utility could be further extended
 54 via coupling to investigate sediment erosion and potentially forecast postfire transport models
 55 and/or ensemble-based operational weather forecasts. Given the high-fidelity performance of our
 56 augmented version of WRF-Hydro, as well as its potential usage in probabilistic hazard forecasts,
 57 we argue for its continued development and application in post-fire hydrologic hazards at regional
 58 scales and natural hazard assessments.

59

60 **Short Summary**

61 In January 2021 a storm triggered numerous debris flows in a wildfire burn scar, California. We
 62 use a hydrologic model to assess debris flow susceptibility in pre-fire and postfire scenarios.
 63 Compared to pre-fire conditions, postfire simulation yields dramatic increases in total and peak
 64 discharge, substantially increasing debris flow susceptibility. Our work proves the 3-D hydrologic
 65 models' utility to investigate and potentially forecast postfire debris flow susceptibility at regional
 66 scales.~~In January 2021 a storm triggered numerous debris flows in a wildfire burn scar in~~
 67 ~~California. We use a hydrologic model to assess debris flow hazards in pre fire and postfire~~
 68 ~~scenarios. Compared to pre fire conditions, the postfire simulation yields dramatic increases in~~

Formatted: Space Before: 12 pt, After: 6 pt, Keep with next

~~total and peak discharge, substantially increasing debris flow hazards. Our work demonstrates the utility of 3-D hydrologic models for investigating and potentially forecasting postfire debris flow hazards at regional scales.~~

1 Introduction

Following intense rainfall, areas with wildfire burn scars are more prone to flash flooding (Neary et al., 2003; Bart & Hope 2010; Bart 2016) and runoff-generated debris ~~flow hazards~~flows than unburned areas (Moody et al., 2013; Ice et al., 2004; Shakesby & Doerr, 2006; Moody et al., 2013). After wildfire, reduced tree canopy interception, decreased soil infiltration due to soil-sealing effects (Larsen et al., 2009), and increased soil water repellency – especially in hyper-arid environments (Dekker ~~and~~ Ritsema, 1994; Doerr ~~and~~ Thomas, 2000; MacDonald ~~and~~ Huffman, 2004) – increases excess surface water, and on sloped terrains leads to overland flow (Shakesby & Doerr, 2006; Stoof et al., 2012). As water moves down hillslopes and erosion adds sediment to water-dominated flows, clear water floods can transition to turbulent and potentially destructive debris flows (Meyer & Wells, 1997; Cannon et al., 2001, 2003; Santi et al., 2008). In contrast to debris flows initiated by shallow landslides, this rainfall-runoff process has been identified as the major cause for postfire debris flows in the western U.S. (Cannon, 2001; Cannon et al., 2003, 2008; Kean et al., 2011; Nyman et al., 2015; Parise & Cannon, 2012; Nyman et al., 2015), and in other regions with Mediterranean climates (Bisson et al., 2005; Mitsopoulos & Mironidis, 2006; BissonRosso et al., 20052007; Parise & Cannon, 2008, 2009; Rosso et al., 2007). In California, because climate change is projected to increase the intensity and frequency of wet-season precipitation (Swain et al., 2018; Polade et al., 2017; Swain et al., 2018), increase wildfire potential (Swain, 2021; Brown et al., 2020; Swain, 2021), and extend the wildfire season (Goss et al., 2020), occurrence and intensity of postfire debris flows are likely to increase (Cannon et al., & DeGraff, 2009; Kean & Staley, 2021; Oakley, 2021).

~~Due to this increasing threat, the development of tools to~~ assess postfire debris flow susceptibility and hazards ~~is critical. However, due to long-standing terminology ambiguity in the natural hazard community (Reichenbach et al., 2018), we first begin with a definition of terms. In this study we demonstrate the use of a new physics-based tool to map postfire debris flow susceptibility at regional scales. We follow the guidance of [Reichenbach et al., (2018) & references therein] and define susceptibility as the likelihood of debris flow occurrence in an area, and hazard as the probability of debris flow occurrence of a given magnitude within a specified area and period of time. In other words, debris flow susceptibility does not estimate debris flow size or consider the timing or frequency of the debris flow occurrence. Rather, it focuses on locating areas prone to debris flows considering local environmental factors (Brabb 1985; Guzzetti et al., 2005).~~

~~Heuristic, deterministic, statistical approaches including empirical, and coupled deterministic and statistical models and machine learning techniques are have previously been employed to assess~~

Formatted: Font color: Black

107 landslide susceptibility (Dahal et al., 2008; Regmi et al., 2010; Park et al., 2016; Reichenbach et
108 al., 2018). For postfire debris flow susceptibility or hazard assessment, however, the use of
109 deterministic models is limited. In contrast, statistical approaches are commonly used in both
110 research and operational settings (Cannon et al., 2010; Friedel 2011a, 2011b; Gardner et al., 2014;
111 Cannon et al., 2010; Staley et al., 2016; Cui et al., 2019; Nikolopoulos et al., 2018; Friedel 2011a,
112 2011b). Statistical approaches are useful for identifying and characterizing relationships amongst
113 contributing environmental factors and are helpful in operational settings due to low computational
114 costs and the potential for rapid assessment.2018; Cui et al., 2019). For example, rainfall intensity-
115 duration (ID) thresholds are one of the simplest-to-implement and most widely used statistical
116 methods for mapping rainfall-induced landslide susceptibility including postfire debris flows
117 (Cannon et al., 2011; Staley et al., 2017). In addition, the U.S. Geological Survey (USGS) currently
118 employs a statistical approach in their Emergency Assessment of Postfire Debris-flow Hazards
119 that consists of a logistic regression model to predict the likelihood of post-wildfire debris flows
120 (e.g., Cannon et al., 2010; Staley et al., 2016; Cannon et al., 2010), and a multiple linear regression
121 model to predict debris flow volumes (Gartner et al., 2014). Machine-learning techniques such as
122 self-organizing maps, genetic programming, and a random forest algorithm have also been used to
123 predict postfire debris flows in the western U.S. (Friedel 2011a, 2011b; Nikolopoulos et al., 2018;
124 Friedel 2011a, 2011b). For example, self-organizing maps and genetic programming were). In
125 general, statistical approaches are useful for identifying and characterizing relationships amongst
126 contributing environmental factors and are widely used due to predict postfire debris flow
127 occurrence (Friedel 2011b) and volumes (Friedel 2011a), respectively. Compared to their low
128 computational costs and the current USGS predictive models, genetic programming was posited
129 to be more useful in solving non-linear multivariate problems (Friedel 2011a), while a random
130 forest algorithm demonstrated increased performance in predicting postfire debris flow occurrence
131 (Nikolopoulos et al., 2018);potential for rapid assessment. Despite the utility and advantages of
132 data-driven hazard prediction approaches over regional domains, these techniques (1) do not
133 simulate the underlying physics, which limits(2) often require large amount of historical
134 observation data that may not be readily available, and (3) result in models that are often only
135 applicable to specific locales. These limitations inhibit their utility in developing a better process-
136 based understanding of debris flow mechanics, limitslimit their applicability in climatological and
137 geographic settings different than their training sites, and limitslimit their use in non-stationary
138 conditions (e.g., under changing climatic conditions).

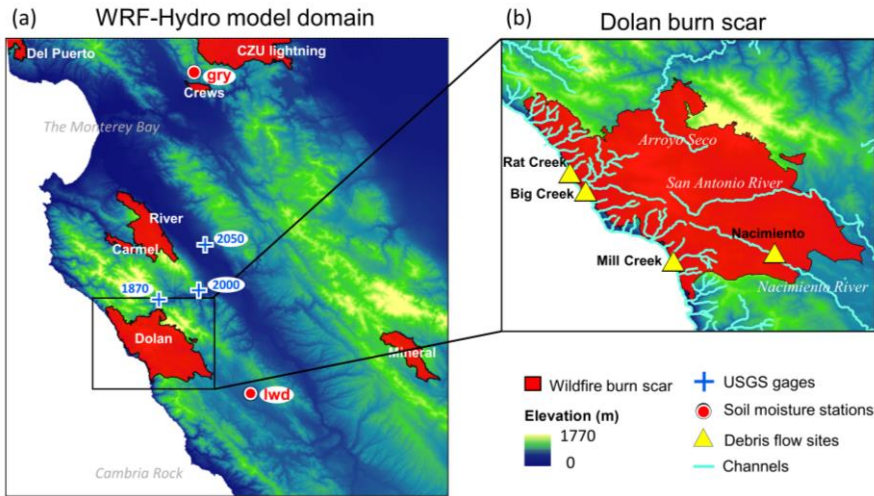
139 In contrast, physics-based models that simulate spatially-explicit hydrologic and mass wastage
140 processes are well-suited for mechanistic sensitivity analyses in diverse settings, ~~but applications~~
141 ~~of these. However, studies employing deterministic process-based~~ models have tended to focus on
142 modeling rainfall-induced shallow landslides (Crosta & Frattini, 2003; Claessens et al., 2007) or
143 landslide-induced debris flows (e.g., Iverson & George, 2014; George & Iverson, 2014), rather
144 than on runoff-generated debris flows which are more common in postfire areas (Cannon et al.,
145 2001, 2003; Santi et al., 2008). Studies that have investigated postfire hydrologic responses using
146 processphysics-based models have largely focused on short-term responses in individual

147 ~~catchments~~ at high spatiotemporal resolutions ([Rengers et al., 2016](#); McGuire et al., 2016, 2017;
148 [Rengers et al., 2016](#)) or long-term runoff responses at coarse temporal resolutions ([Rulli & Rosso,
149 2007](#); [McMichael & Hope, 2007](#)); [Rulli & Rosso, 2007](#)) ~~in individual catchments rather than~~
150 ~~assessing susceptibility over regional domains~~. For example, process-based models have employed
151 shallow water equations to understand the triggering and transport mechanisms of postfire debris
152 flows in single catchments (McGuire et al., 2016, 2017) and to investigate the timing of postfire
153 debris flows in three separate catchments (Rengers et al., 2016), the latter of which also assessed
154 the efficacy of a simplified kinematic wave approach. In addition to individual catchment
155 applications, process-based models often adopt simplifications that can limit effective prediction
156 and hypothesis testing to overcome computational limits. For example, the kinematic runoff and
157 erosion model (KINEROS2) simplifies drainage basins into 1-dimensional channels and hillslope
158 patches ([Canfield & Goodrich, et al., 2005](#); [Goodrich et al., 2012](#); [Sidman et al., 2015](#)~~2016~~), and
159 the Hydrologic Modeling System (HEC-HMS) uses an empirically-based curve number method
160 to estimate saturation excess water ([Cydzik et al., 2009](#)), which cannot resolve infiltration excess
161 overland flow, a critical process in burn scars ([Chen et al., 2013](#)).

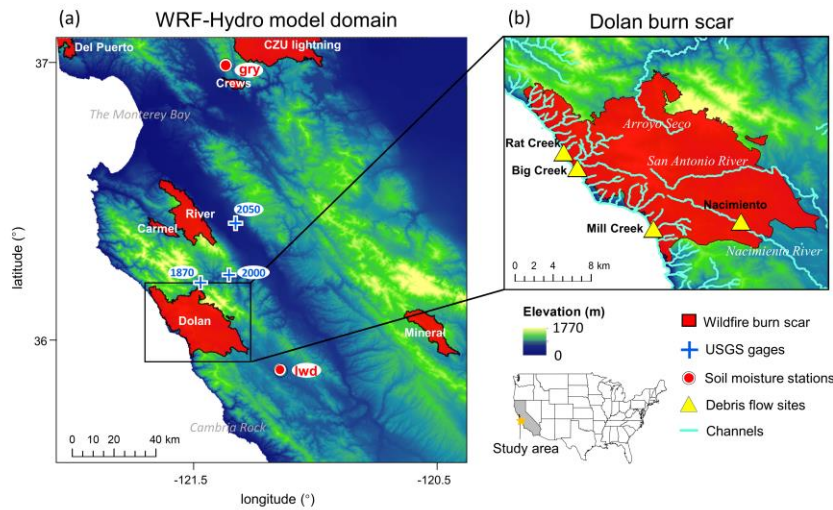
162 Given the current state of debris flow ~~hazard~~~~susceptibility~~ assessment and prediction in previously
163 burned terrains, in addition to the growing influence of anthropogenic climate change on wildfire
164 and extreme precipitation, development of physics-based ~~hazard~~ ~~assessments~~~~susceptibility~~
165 ~~mapping~~ tools that can be used in both hindcast investigations and forecasting applications is
166 needed. Furthermore, due to the diverse morphology ~~and often large spatial scales~~ of precipitation
167 events and their ~~interaction~~~~interactions~~ with geographically distributed wildfire burn scars,
168 development of tools that can assess ~~hazard~~~~susceptibility~~ over regional domains, particularly in
169 operational forecasting applications, is critical. Here, ~~to~~ advance the field of burn scar debris flow
170 ~~hazard~~~~susceptibility~~ assessment, we explore the use of the physics-based and fully-distributed
171 Weather Research and Forecasting Hydrological modeling system version 5.1.1 (WRF-Hydro).
172 WRF-Hydro is an open-source community model developed by the National Center for
173 Atmospheric Research (NCAR). It is the core of ~~the~~ National Oceanic and Atmospheric
174 Administration's (NOAA) National Water Model forecasting system, and has been used
175 extensively to study channelized flows ~~over regional domains~~ (e.g., [Wang et al., 2019](#); [Lahmers et
176 al., 2020](#); [Wang et al., 2019](#)). Here, we modify WRF-Hydro to output high temporal resolution
177 fine-scale (100 m) debris flow-relevant overland flow; a process computed using a fully unsteady,
178 explicit, finite difference diffusive wave formulation. Previous efforts, employing shallow water
179 equations, diffusive, kinematic, and diffusive-kinematic wave models, have demonstrated that
180 water-only models can provide critical insights on runoff-driven debris flow behavior ([Arattano &
181 Savage, 1994](#); [McGuire & Youberg, 2020](#); [Arratano & Franzi, 2010](#); [Di Cristo et al., 2021](#)), even
182 in burned watersheds ([Rengers et al., 2016](#); [McGuire & Youberg, 2020](#)).

183 To test and demonstrate the utility of WRF-Hydro in debris flow studies, we investigate the
184 January 2021 debris flow events within the Dolan burn scar on the Big Sur coast of central
185 California (Fig. 1a–b). We first identify multiple debris flow sites using optical and radar remote
186 sensing data and field investigations. We then calibrate WRF-Hydro against ground-based soil

187 moisture and streamflow observations and use it to study the effects of burn scars on debris flow
 188 hydrology and ~~changes in hazard potential susceptibility~~. The paper is organized as follows.
 189 Section 2 describes ~~our debris flow~~the identification approach and ~~historical context~~geologic
 190 ~~setting of debris flows~~. Section 3 presents a description of WRF-Hydro. Section 4 describes the
 191 simulation, calibration, and validation of WRF-Hydro. Section 5 presents the results. Section 6
 192 discusses the results and Sect. 7 provides a conclusion.



193



194

195 **Fig. 1|** WRF-Hydro model domain and Dolan burn scar. (a) WRF-Hydro model domain depicting
 196 topography, 2020 wildfire season burn scars, and PSL soil moisture and USGS stream gage
 197 observing sites. The black rectangle outlines (b) the Dolan burn scar inset, in which debris flow
 198 locations and major streams are marked and labeled. The location of the study area is shown in the
 199 embedded U.S. map with the state of California shaded in grey.

200

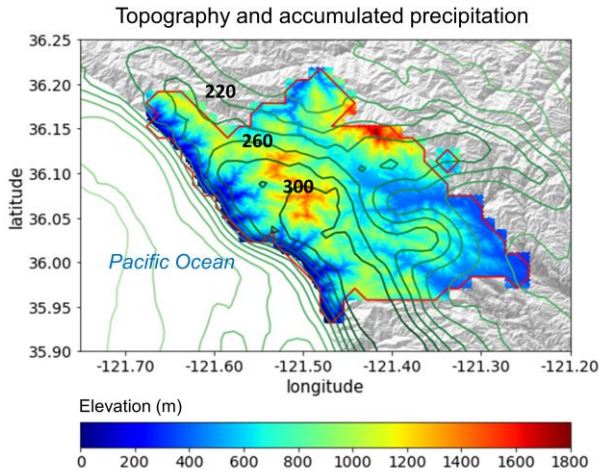
201

202 **2 Study domain and debris flow identification methodology**

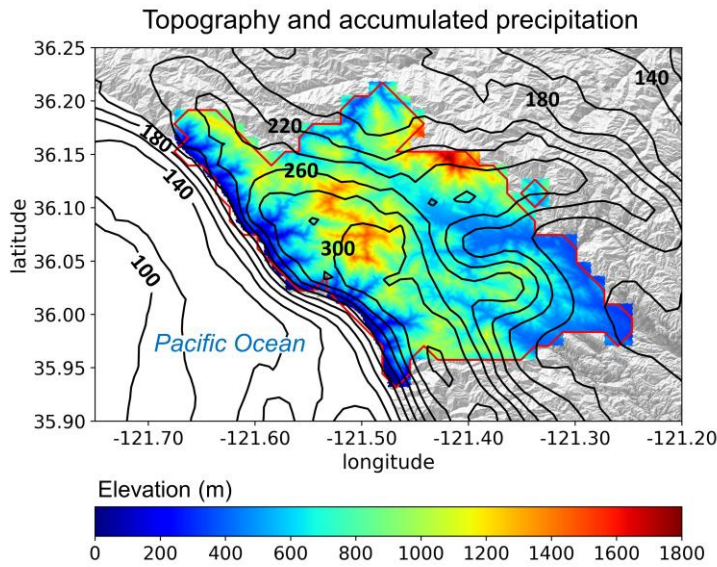
203 The Dolan wildfire burned from August 18th till December 31st, 2020. 55% of areas within the fire
 204 perimeter were burned at moderate-to-high severity (Burned Area Emergency Response, 2020).
 205 After the fire, USGS Emergency Assessment of Postfire Debris-flow Hazards produced a debris
 206 flow hazard assessment using a design storm based statistical model (USGS, 2020). On January
 207 27–29, 2021, an atmospheric river (AR) made landfall on the Big Sur coast, bringing more than
 208 300 mm of rainfall to California’s Coast Ranges (Fig. 2), with a peak rainfall rate of 24 mm h⁻¹.
 209 During the AR event, a section of California State Highway 1 (CA1) at Rat Creek was destroyed
 210 by a debris flow. CA1 was subsequently closed for three months and rebuilt at a cost of ~\$11.5M
 211 (Los Angeles Times, 2021).

212

213



214



215

216

217

218

219

Fig. 2| The topography (shading; m) and MRMS accumulated precipitation (contour lines; mm) during the AR event from January 27th 00:00 to 29th 23:00 in the Dolan burn scar. Contour line interval for accumulated precipitation is 20 mm, and lines of 100, 140, 180, 220, 260, and 300 mm are labeled. The red polygon outlines the perimeter of the Dolan burn scar.

Formatted: Font: Bold, Font color: Auto

Formatted: Justified, Space Before: 0 pt, Border: Top: (No border), Bottom: (No border), Left: (No border), Right: (No border), Between : (No border)

220
221

222 2.1 Debris flow identification from remote sensing and field work

223 In addition to the Rat Creek debris flow, which made national news (Los Angeles Times, 2021),
224 we identified three other debris flows using a combination of field investigation, and open access
225 satellite optical and synthetic aperture radar (SAR) images (Fig. 3 and Fig. B1).

226 We examined relative differences in normalized difference vegetation index (rdNDVI) defined by
227 (Scheip & Wegmann, 2021):

$$228 \quad rdNDVI = \frac{NDVI_{post} - NDVI_{pre}}{\sqrt{NDVI_{pre} + NDVI_{post}}} \times 100 \quad (1)$$

229 where $NDVI_{pre}$ and $NDVI_{post}$ are the pre- and post-event normalized difference vegetation index
230 (NDVI) images computed following:

$$231 \quad NDVI = \frac{NIR - Red}{NIR + Red} \quad (2)$$

232 where NIR is the near-infrared response and Red is the visible red response. rdNDVI was calculated
233 from Sentinel-2 satellite data using the HazMapper v1.0 Google Earth Engine application (Scheip
234 & Wegmann, 2021). HazMapper requires selection of an event date, pre-event window (months),
235 post-event window (months), max cloud cover (%) and slope threshold ($^{\circ}$). These input
236 requirements filter the number of images used to calculate the rdNDVI. We set the event date to
237 ~~27~~ January 27th, 2021 and used a 3 month pre- and post-event window with 0% max cloud cover
238 and a 0° slope threshold to identify vegetation loss associated with the debris flows. We then
239 created a binary map to highlight debris flows (and other vegetation loss) pixels above a rdNDVI
240 vegetation loss threshold. We removed all pixels with $rdNDVI > -10$.

241 Lastly, we searched for debris flows (and other ground surface deformation) by examining SAR
242 backscatter change with data acquired by the Copernicus Sentinel-1 (S1) satellites (see full
243 description in Handwerger et al., ~~in review~~, (2022)). We measured the change in SAR backscatter
244 by using the log ratio approach, defined as

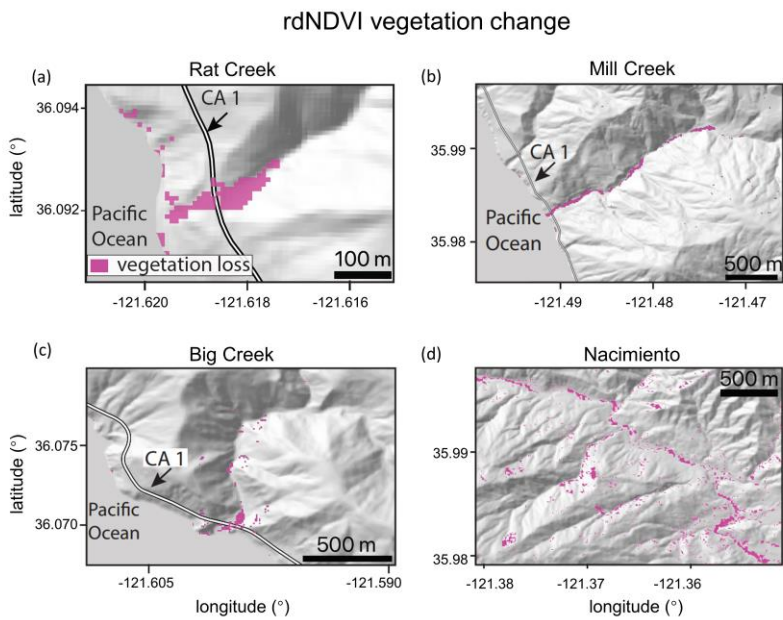
$$245 \quad I_{ratio} = 10 \times \log_{10} \left(\frac{\sigma_{pre}^0}{\sigma_{post}^0} \right) \quad (3)$$

246 where σ_{pre}^0 is a pre-event image stack (defined as the temporal median) of SAR backscatter and
247 σ_{post}^0 is a post-event image stack. Similar to the HazMapper method, our approach requires
248 selection of an event date, pre-event window (months), post-event window (months) and slope
249 threshold ($^{\circ}$). No cloud-cover threshold is needed since SAR penetrates clouds. We used a 3 month
250 pre- and post-event window and 0° slope threshold to identify ground surface changes associated
251 with the debris flows. We then created a binary map to highlight debris flows by removing all
252 pixels with $I_{ratio} < 99^{\text{th}}$ percentile value: ~~threshold suggested by Handwerger et al. (2022)]~~.

Formatted: Superscript

253 Identified debris flow source areas and deposition sites were confirmed by field investigation (N.J.
 254 Finnegan) and named after the locations where they deposited (i.e., Big Creek, Mill Creek, and
 255 Nacimiento). ~~We note that there were likely more debris flows triggered during the AR event.~~
 256 ~~However, given the primary goal of this study—to demonstrate the utility of WRF-Hydro—a~~
 257 ~~comprehensive cataloging of debris flows is beyond this study’s scope.~~

258



259
 260 **Fig. 3|** Identified debris flow sites using rdNDVI vegetation change within the Dolan burn scar.
 261 We convert the rdNDVI data into a binary map by setting a threshold value, which ~~yield~~
 262 only the likely debris flow locations ~~and drape these maps over a topographic hillshade.~~ (a)–(d)
 263 Sentinel-2 rdNDVI vegetation change at (a) Rat Creek, (b) Mill Creek, (c) Big Creek, and (d) the
 264 Nacimiento River.

265

266 **2.2 Debris flow geologic setting**

267 According to the USGS National Elevation Dataset 30-m digital elevation model (DEM), the Rat
 268 Creek debris flow sits at the base of a 1st order catchment with a drainage area of 2.23 km². Mill
 269 Creek, Big Creek, and Nacimiento debris flows were initiated within extremely steep, intensely
 270 burned, 1st order catchments, but were deposited in 2nd, 3rd, and 3rd Strahler stream order channels.

271 respectively. All four debris flows were channelized. Rat Creek, Mill Creek, and Big Creek debris
272 flow deposition sites have elevations ranging from 20–60 m, while Nacimiento debris flow
273 deposited at an elevation of ~440 m above sea level. We calculate catchment slopes using the DEM
274 and the slope calculation function in ArcMap. The average slope of the catchments containing Rat
275 Creek and Mill Creek debris flow deposition sites is ~25°. The average catchment slope of Big
276 Creek deposition site is ~28° and Nacimiento is ~21°. For debris flow source areas, the average
277 and maximum slopes of Mill Creek are 23° and 39°, 21° and 43° for Big Creek, and 24° and 41°
278 for Nacimiento. According to the Soil Survey Geographic Database and California geologic map
279 data, surface soils at the three coastal debris flow sites (i.e., Rat Creek, Mill Creek, and Big Creek)
280 are texturally classified as loam with underlying Franciscan Complex sedimentary rocks of
281 Jurassic to Cretaceous age. Soil at Nacimiento is classified as sandy loam with underlying Upper
282 Cretaceous and Paleocene marine sedimentary rocks from the Dip Creek Formation, Asuncion
283 Group, Shut-In Formation, Italian Flat Formation, Steve Creek Formation, and El Piojo Formation.
284 Mill Creek, Big Creek, and Nacimiento were relatively large debris flows with runout lengths
285 between ~2–5 km, while Rat Creek occurred in a smaller catchment and had a runout length of
286 ~300 m. The difference in runout length and debris flow size is primarily controlled by upstream
287 catchment size, however for the three coastal debris flow events at Rat Creek, Big Creek, and Mill
288 Creek, also constrained by the downslope ocean. We note that there were likely more debris flows
289 triggered during the AR event. The four debris flow events highlighted here were identified during
290 brief post-event field excursions due to their intersection with major roadways. Given that our
291 primary goal here is to demonstrate the utility of WRF-Hydro – a comprehensive catalogue of
292 debris flows is beyond the scope of this study, although underway by other researchers (Cavagnaro
293 et al., 2021).

294 **3 WRF-Hydro**

295 **3.1 Model description**

296 WRF-Hydro is an open-source physics-based community model that simulates land surface
297 hydrologic processes. It includes the Noah-Multiparameterization (Noah-MP) land surface model
298 (LSM; Niu et al., 2011), terrain routing module, channel routing module, and a conceptual
299 baseflow bucket model. The Noah-MP LSM is a 1-dimensional column model that calculates
300 vertical energy fluxes (i.e., sensible and latent heat, net radiation), moisture (i.e., canopy
301 interception, infiltration, infiltration excess, deep percolation), and soil thermal and moisture states
302 on the LSM grid (1 km in our application). The infiltration excess, ponded water depth, and soil
303 moisture are then disaggregated using a time-step weighted method (Gochis & Chen, 2003) and
304 sent to the terrain routing module which simulates subsurface and overland flows on a finer terrain
305 routing grid (100 m in our application). According to the mass balance, local infiltration excess,
306 overland flow, and exfiltration from baseflow contribute to the surface head which flows into river
307 channels if defined retention depth is exceeded. The channel routing module then calculates
308 channelized flows assuming a trapezoidal channel shape (Fig. B2). Parameters related to the

309 trapezoidal channel, such as channel bottom width (B_w), Manning's roughness coefficient (n), and
 310 channel side slope (z) are functions of channel stream order (Fig. B3 and Table B1). Computed
 311 streamflow is then output on the 100 m grid. Equations used to compute infiltration excess,
 312 overland flow, and channelized flow are provided in Sect. 3.3 and 3.4.

313 By default, WRF-Hydro uses Moderate Resolution Imaging Spectroradiometer (MODIS)
 314 Modified International Geosphere-Biosphere Program (IGBP) 20-category land cover product as
 315 land cover (Fig. B4) and 1-km Natural Resources Conservation Service State Soil Geographic
 316 (STATSGO) database for soil type classification (Fig. B5; Miller & White, 1998). Land surface
 317 properties including canopy height (HVT), maximum carboxylation rate (VCMX25), and overland
 318 flow roughness (OV_ROUGH2D) are functions of land cover type (Table B2 & Fig. B4). Default
 319 soil hydraulic parameters in WRF-Hydro (i.e., soil porosity, grain size distribution index, and
 320 saturated hydraulic conductivity) are based on Cosby et al.'s (1984) soil analysis (Table B3) and
 321 are used to map onto the STATSGO 16 soil texture types (Fig. B5).

322

323 3.2 Meteorological forcing files

324 WRF-Hydro is used in [a](#) standalone mode (i.e., it is not interactively coupled with the atmospheric
 325 component of WRF), but rather is forced with a combination of Phase 2 North American Land
 326 Data Assimilation System (NLDAS-2) meteorological data and Multi-Radar/Multi-Sensor System
 327 (MRMS) radar-only quantitative precipitation (Zhang et al., 2011, 2014, 2016). A description of
 328 the MRMS dataset and uncertainties therein can be found in Appendix A. NLDAS-2 provides
 329 hourly forcing data including incoming shortwave and longwave radiation, 2-m specific humidity
 330 and air temperature, surface pressure, and 10-m wind speed at 1/8-degree spatial resolution.
 331 MRMS provides hourly precipitation ~~rates~~ at 1-km resolution.

332

333 3.3 Overland flow routing and output

334 The Noah-MP LSM calculates rate of infiltration excess following Chen & Dudhia (2001):

335

$$336 \quad \frac{\partial h}{\partial t} = \frac{\partial P_d}{\partial t} \left\{ 1 - \frac{[\sum_{i=1}^4 \Delta D_i (\theta_s - \theta_i)] \left[1 - \exp \left(-k \frac{K_s}{K_{ref}} \delta t \right) \right]}{P_d + [\sum_{i=1}^4 \Delta D_i (\theta_s - \theta_i)] \left[1 - \exp \left(-k \frac{K_s}{K_{ref}} \delta t \right) \right]} \right\} \quad (4)$$

337

338 where h (m) is the surface water depth and t is the time. P_d (m) is the precipitation not intercepted
 339 by the canopy; ΔD_i (m) is the depth of soil layer i ; θ_i is the soil moisture in soil layer i ; θ_s is the
 340 soil porosity; K_s (m s^{-1}) is the saturated hydraulic conductivity; K_{ref} is $2 \times 10^{-6} \text{ m s}^{-1}$ which
 341 represents the saturated hydraulic conductivity of the silty-clay-loam soil texture chosen as a

342 reference; δ_t (s) is the model time step; and k which is equal to 3.0 is the runoff–infiltration
343 partitioning parameter [the same as kdt_{ref} in Chen & Dudhia (2001)].

344

345 Noah-MP passes excess water to the terrain routing module, which simulates overland flow using
346 a 2-dimensional fully-unsteady, explicit, finite-difference diffusive wave equation adapted from
347 Julien et al. (1995) and Ogden (1997). It is considered ~~superior~~ improved compared to the
348 traditionally used kinematic wave formulation in that it accounts for backwater effects and flow
349 over adverse slopes. The diffusive wave formulation is the simplified form of the Saint Venant
350 equations, i.e., continuity and momentum equations for a shallow water wave. The 2-dimensional
351 continuity equation for a flood wave is:

$$352 \quad \frac{\partial h}{\partial t} + \frac{\partial q_x}{\partial x} + \frac{\partial q_y}{\partial y} = i_e \quad (5)$$

353 where h is the surface flow depth, q_x and q_y are the unit discharges in the x- and y-directions,
354 respectively, and i_e is the infiltration excess. Manning's equation which considers momentum loss
355 is used to calculate q . In the x-direction:

$$356 \quad q_x = \alpha_x h^\beta \quad (6)$$

357 Where β is a unit dependent coefficient equal to $\frac{5}{3}$, and

$$358 \quad \alpha_x = \frac{S_{fx}^{1/2}}{n_{ov}} \quad (7)$$

359 where n_{ov} is the tunable overland flow roughness coefficient. The momentum equation in the x-
360 direction is given by:

$$361 \quad S_{fx} = S_{ox} - \frac{\partial h}{\partial x} \quad (8)$$

362 where S_{fx} is the friction slope, S_{ox} is the terrain slope, and $\frac{\partial h}{\partial x}$ is the change in surface flow depth
363 in the x-direction.

364 Off-the-shelf, WRF-Hydro does not output overland flow at terrain routing grids (100 m), however
365 it is computed in the background to determine channelized streamflow. One key advance made in
366 this work is that we modified WRF-Hydro source code to output overland flow. Overland flow
367 depth (m) was converted to overland discharge ($m^3 s^{-1}$) by multiplying flow depth by grid cell area
368 ($10,000 m^2$) and dividing by the LSM time step (1 h).

369

370 **3.4 Channel routing**

371 If overland flow intersects grid cells identified as channel grids ~~f~~(2nd Strahler stream order and
372 above; pre-defined by the hydrologically conditioned USGS ~~National Elevation Dataset 30 m~~

373 ~~digital elevation model (30-m DEM)~~, the channel routing module routes the water as
374 channelized streamflow using a 1-dimensional, explicit, variable time-stepping diffusive wave
375 formulation. Similarly, the continuity equation for channel routing is given as:

$$376 \quad \frac{\partial A}{\partial t} + \frac{\partial Q}{\partial s} = q_l \quad (9)$$

377 and the momentum equation is given as:

$$378 \quad \frac{\partial Q}{\partial t} + \frac{\partial(\gamma \frac{Q^2}{A})}{\partial s} + gA \frac{\partial H}{\partial s} = -gAS_f \quad (10)$$

379 where s is the streamwise coordinate, H is water surface elevation, A is the flow cross-sectional
380 area calculated as $(B_w + H z)H$ (Fig. B2), q_l is the lateral inflow rate into the channel grid, Q is
381 the flow rate, γ is a momentum correction factor, g is acceleration due to gravity, and S_f is the
382 friction slope computed as:

$$383 \quad S_f = \left(\frac{Q}{K}\right)^2 \quad (11)$$

384 where K is the conveyance computed from the Manning's equation:

$$385 \quad K = \frac{C_m}{n} AR^{2/3} \quad (12)$$

386 where n is the Manning's roughness coefficient, A is the channel cross-sectional area, R is the
387 hydraulic ~~radius~~radius (A/P), P is the wetted perimeter, and C_m is a dimensional constant (1.486
388 for English units or 1.0 for SI units).

389

390 **4 Model simulation, calibration, and validation**

391 **4.1 Model domain**

392 The WRF-Hydro model domain spans regions in California including the Coast Ranges, Monterey
393 Bay, and the Central Valley, and covers several burn scars from the 2020 wildfire season (Fig. 1a).
394 Here we focus our analysis on the Dolan burn scar where the hazardous debris flows occurred (Fig.
395 1b). ~~According to the USGS 30 m DEM, the Rat Creek debris flow site sits at the base of a 1st
396 order catchment with a drainage area of 2.23 km². Mill Creek, Big Creek, and Nacimiento debris
397 flows were initiated within extremely steep, intensely burned, 1st-order catchments, but were
398 deposited in 2nd, 3rd, and 3rd Strahler stream order channels, respectively.~~

399 To calibrate and validate WRF-Hydro output, we use soil moisture observations from two Physical
400 Sciences Laboratory (PSL) monitoring stations [i.e., Lockwood (lwd) and Gilroy (gry)] (Fig. 1a).
401 Due to the Mediterranean climate of California, many USGS stream gages experience low or no
402 flow during the dry season. In addition, many gages are under manual regulation to mitigate wet-
403 season flood risks and better distribute water resources. As such, it can be challenging to obtain
404 natural streamflow observations for model calibration. Here, three USGS stream gages [i.e.,

405 Arroyo Seco NR Greenfield, CA (ID 11151870), Arroyo Seco NR Soledad, CA (ID 11152000),
406 and Arroyo Seco BL Reliz C NR Soledad, CA (ID 11152050)] (Fig. 1a) on streams that have
407 measurable flows during our study period and are free of human regulation are used. These gages
408 are located downstream of the Dolan burn scar and hence are useful in calibrating the parameters
409 associated with burn scar effects. The PSL soil moisture observations were recorded at 2-minute
410 intervals and USGS streamflow gage data were recorded at 15-minute intervals, but we perform
411 all observation-model comparisons at hourly-mean resolution.

412

413

414 4.2 Baseline simulation and soil moisture calibration

415 WRF-Hydro was [initialized with National Centers for Environmental Prediction \(NCEP\) FNL](#)
416 [\(Final\) Operational Global Analysis data and was run](#) from January 1–31 ~~of~~, 2021. We performed
417 the baseline simulation by modifying WRF-Hydro default parameters (Table B3) based on a
418 calibration using soil moisture observations from stations lwd and gry. Neither PSL station is
419 located in a burn scar. Since the baseline simulation includes no postfire characteristics, it can also
420 be regarded as the “pre-fire” scenario. Soil moisture at 10 cm below ground in the baseline
421 simulation was calibrated by performing a domain-wide adjustment of soil porosity and grain size
422 distribution index at the simulation start (Table B3). We then allowed the model to spin up from
423 January 1–10 before using January 11–31 for validation. Using a relatively short spin-up period is
424 justified because prior to the AR event, little rain fell on the Dolan burn scar (i.e., ~400 mm of
425 rainfall fell from June to December 2020). As such, in the months preceding the debris flow events,
426 soil moisture observations indicate already dry ~~condition~~[conditions](#) prior to our 10 day spin up.

427

428 After calibration, the simulated soil moisture closely mimics ground-based PSL observations (Fig.
429 4). Both the observed magnitude and variability are well captured, with the simulated ± 1 standard
430 deviation envelope largely encompassing PSL observations during the AR. Model performance
431 was evaluated using four quantitative metrics, i.e., correlation coefficient ~~(r)~~, root mean square
432 error ~~(RMSE)~~, mean ~~bias~~[absolute error \(MAE\)](#), and Kling-Gupta efficiency (KGE; Gupta et al.,
433 2009; Kling et al., 2012). KGE has previously been used in soil moisture calibration applications
434 (e.g., Lahmers et al., 2019; Vergopolan et al., 2020) and is computed as follows:

435

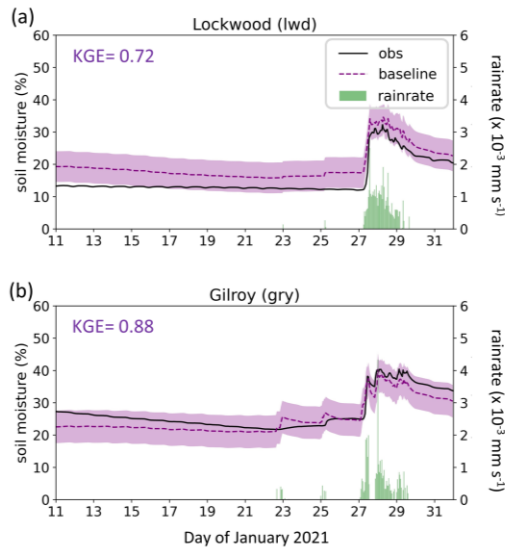
$$436 \quad KGE = 1 - \sqrt{(r - 1)^2 + (\alpha - 1)^2 + (\beta - 1)^2} \quad (13)$$

437

438 where r is the correlation coefficient between the observation and simulation, α is the ratio of the
439 standard deviation of simulation to the standard deviation of observation, and β is the ratio of the
440 mean of simulation to the mean of observation. KGEs close to 1 indicate a high-level consistency
441 between the simulation and observation, while negative KGEs indicate poor model performance
442 ([Andersson et al., 2017](#); [Schönfelder et al., 2017](#); [Andersson et al., 2017](#)).

443
 444 The model's ability to simulate soil moisture substantially improves after calibration (Fig. 4; Table
 445 1). KGE values approach 1 (0.72 at lwd and 0.88 at gry), indicating that WRF-Hydro adequately
 446 simulates the hydrologic environment and its response to meteorological changes.
 447
 448
 449

MRMS precipitation, observed and simulated soil moisture



450
 451 **Fig. 4|** Precipitation, observed and simulated soil moisture at two PSL soil moisture stations.
 452 January 11–31, 2021 MRMS precipitation (green bars) and observed (black line) and simulated
 453 volumetric soil moisture 10 cm below ground in the baseline simulation (purple dashed line) at
 454 PSL sites (a) Lockwood (lwd) and (b) Gilroy (gry). Envelope of purple shading depicts ± 1 standard
 455 deviation of model simulated soil moisture. KGE scores are provided at top left for each station.
 456

457
 458
 459 *Table 1*
 460 *Evaluation metrics of simulated soil moisture and streamflow*
 461

Soil moisture (Default / Baseline)				
Station	r	RMSE	BiasMAE	KGE
lwd	0.97 / <u>0.98</u>	7.06 / <u>4.32</u>	5.21 / <u>4.16</u>	0.10 / <u>0.72</u>
gry	0.94 / 0.94	5.19 / <u>2.53</u>	-4.79 / -1.66 <u>1.12 / 2.31</u>	0.80 / <u>0.88</u>

Streamflow (Baseline / Burn scar)				
Station	r	RMSE	BiasMAE	NSE
1870	0.28 / <u>0.93</u>	39.29 / <u>14.69</u>	1.65 / 3.36 <u>16.05 / 6.14</u>	-0.17 / <u>0.84</u>
2000	0.26 / <u>0.86</u>	51.22 / <u>24.92</u>	2.47 / 4.84 <u>20.11 / 10.00</u>	-0.15 / <u>0.73</u>
2050	0.25 / <u>0.81</u>	49.96 / <u>27.43</u>	5.70 / 8.24 <u>19.64 / 11.65</u>	-0.38 / <u>0.53</u>

462
463 **Table 1** | Quantitative evaluation metrics for the simulated soil moisture and streamflow when
464 compared against observations. The metrics include the Pearson correlation coefficient (r), root
465 mean square error (RMSE), and mean ~~bias~~ (Bias):absolute error (MAE). In addition, the
466 comprehensive metrics Kling-Gupta efficiency (KGE) and Nash-Sutcliffe efficiency (NSE) are
467 used to evaluate model-simulated soil moisture and streamflow, respectively. For soil moisture,
468 the numbers in front of “/” are calculated between the default run (i.e., uncalibrated run) and the
469 observations, whereas the numbers following “/” are the corresponding values in the baseline
470 simulation (the purple dashed line in Fig. 4). For streamflow, the numbers in front of “/” are
471 computed between the baseline run (purple dashed line in Fig. 6) and the observations, while the
472 numbers behind “/” are for burn scar simulation (red line in Fig. 6). If the model performance
473 regarding a certain metric is enhanced in the burn scar simulation, the number after “/” is
474 underlined.
475

476 4.3 Burn scar simulation and streamflow calibration

477 To simulate effects of wildfire burn scars on hydrologic processes and debris flow
478 ~~hazard~~ susceptibility, we made two modifications to the baseline simulation soil moisture
479 calibrated model configuration. First, we changed the land cover type within the burn scar
480 perimeter to its nearest LSM analogue, i.e., “barren and sparsely vegetated”. The switch to barren
481 land causes: (1) height of the canopy (HVT) to decrease to 0.5 m; (2) maximum rate of
482 carboxylation at 25°C (VCMX25) to decrease to $0 \mu\text{mol CO}_2/(\text{m}^2 \cdot \text{s})$; and (3) overland flow
483 roughness coefficient (OV_ROUGH2D) to decrease to 0.035 (Fig. 5a–c) from default values (Fig.
484 B4 and Table B2).
485

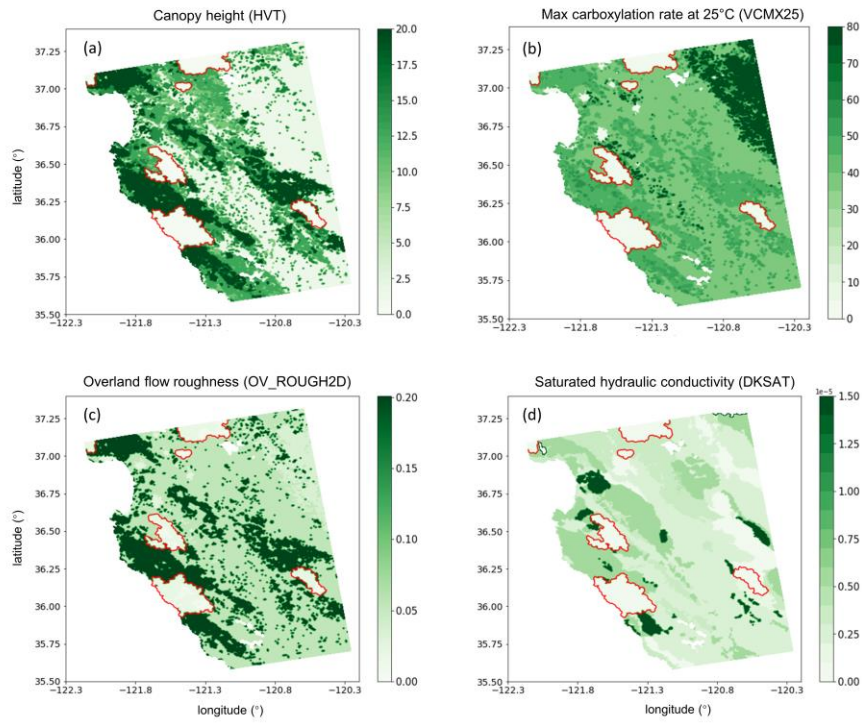
486 The second adjustment was to decrease soil infiltration rates within the burn scar perimeter,
 487 achieved by reducing soil saturated hydraulic conductivity (DKSAT; Fig. 5d; Scott & van Wyk,
 488 1990; Cerdà, 1998; Robichaud, 2000; Martin & Moody, 2001) from default values (Table B3).
 489 Consistent with the hydrophobicity of burned soils, we calibrate the burn scar simulation by
 490 systematically exploring a range of burn scar area saturated hydraulic conductivities (0 to 3×10^{-7}
 491 m s^{-1} with a $5 \times 10^{-8} \text{ m s}^{-1}$ increment), with the goal of reproducing streamflow behavior similar to
 492 USGS gage observations. We found that a value of $1.5 \times 10^{-7} \text{ m s}^{-1}$ gives the highest Nash-Sutcliffe
 493 efficiency (NSE; Nash & Sutcliffe, 1970) across all three USGS stream gages (Table 1). NSE and
 494 KGE are the two most widely used metrics for calibration and evaluation of hydrologic models.
 495 The NSE has previously been used in streamflow calibration applications (e.g., Xia et al., 2012;
 496 Bitew & Gebremichael, 2011), and it is calculated as follows:

$$NSE = 1 - \frac{\sum_{t=1}^{t=T} (Q_{sim}(t) - Q_{obs}(t))^2}{\sum_{t=1}^{t=T} (Q_{obs}(t) - \overline{Q_{obs}})^2} \quad (14)$$

499 where T is the length of the time series, $Q_{sim}(t)$ and $Q_{obs}(t)$ are the simulated and observed
 500 discharge at time t , respectively, and $\overline{Q_{obs}}$ is the mean observed discharge. By definition, NSEs of
 501 1 indicate perfect correspondence between the simulated and observed streamflow. Positive NSEs
 502 ~~mean~~ indicate that the model streamflow has a greater explanatory power than the mean of the
 503 observations, whereas negative NSEs represent poor model performance (e.g., Moriasi et al., 2007;
 504 Schaeffli & Gupta, 2007). When burn scar characteristics are included, evaluation metrics including
 505 r , RMSE, and MAE all improve, while NSEs increase from negative values in the baseline to
 506 greater than 0.584, 0.73, and the NSEs 0.53 at gages 1870 ~~and~~, 2000 ~~reach 0.84,~~ and 0.732050,
 507 respectively. Higher correlation and NSE scores and lower errors indicate the
 508 ~~abovementioned~~ above mentioned burn scar parameter changes improve the model's ability to
 509 simulate streamflow observations downstream of the burn scar (Table 1).

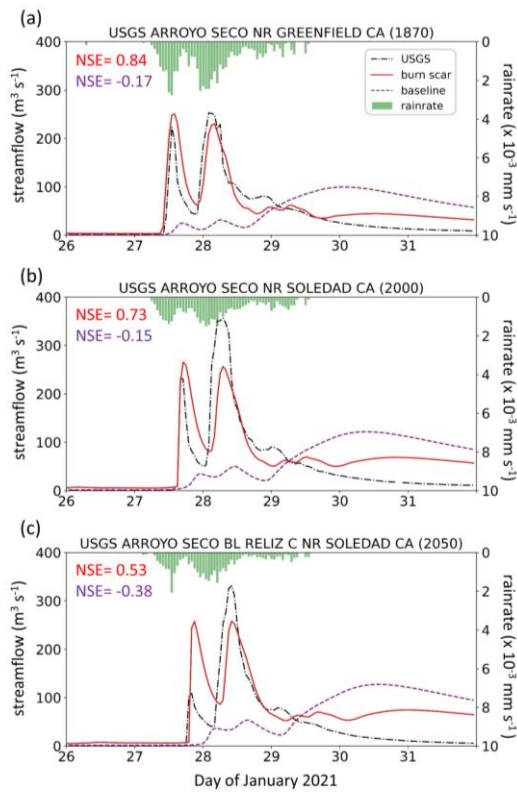
511

Parameter changes accounting for burn scar characteristics



512
513 **Fig. 5|** Parameter setting in the WRF-Hydro burn scar simulation. (a) The height of the canopy
514 (HVT; m; shading), (b) maximum rate of carboxylation at 25°C (VCMX25; $\mu\text{mol CO}_2/(\text{m}^2 \cdot \text{s})$;
515 shading), (c) overland flow roughness coefficient (OV_ROUGH2D; shading), and (d) saturated
516 hydraulic conductivity (DKSAT; m s^{-1} ; shading) in the burn scar simulation.

MRMS precipitation, observed and simulated streamflow



517
 518 **Fig. 6|** Precipitation, observed and simulated streamflow at three USGS stream gages. January 26–
 519 31, 2021 MRMS precipitation (green bars), observed (black dash dotted line) and simulated
 520 streamflow in baseline simulation (purple dashed line) and burn scar simulation (red line) at (a)
 521 Arroyo Seco NR Greenfield, CA (ID 11151870), (b) Arroyo Seco NR Soledad, CA (ID 11152000),
 522 and (c) Arroyo Seco BL Reliz C NR Soledad, CA (ID 11152050). NSE scores for baseline (purple)
 523 and burn scar simulations (red) are shown at top left.
 524

525 **5 Results**

526 **5.1 Hydrologic response due to burn scar incorporation**

527 The pre-fire baseline simulation fails to capture the hydrologic behavior observed at the USGS
528 gages located within the burn scar (Fig. 6). Incorporation of burn scar characteristics substantially
529 alters the hydrologic response of the model and provides much higher fidelity streamflow
530 simulations (Fig. 6). Observed hydrographs are characterized by two early streamflow peaks
531 related to two precipitation bursts on January 27th and 28th. Our burn scar simulation captures this
532 behavior, while the baseline simulation streamflow peaks just once, with a lower magnitude and
533 an ~3-day lag after peak precipitation (Fig. 6). The steep rising limbs and high magnitude discharge
534 peaks of the burn scar hydrograph are indicative of flash flooding. Compared with the pre-fire
535 baseline scenario, the burn scar's barren land and low infiltration rate substantially accelerate
536 drainage rates and increase discharge volume into stream channels.
537

538 **5.2 Hydrologic response at four debris flow sites**

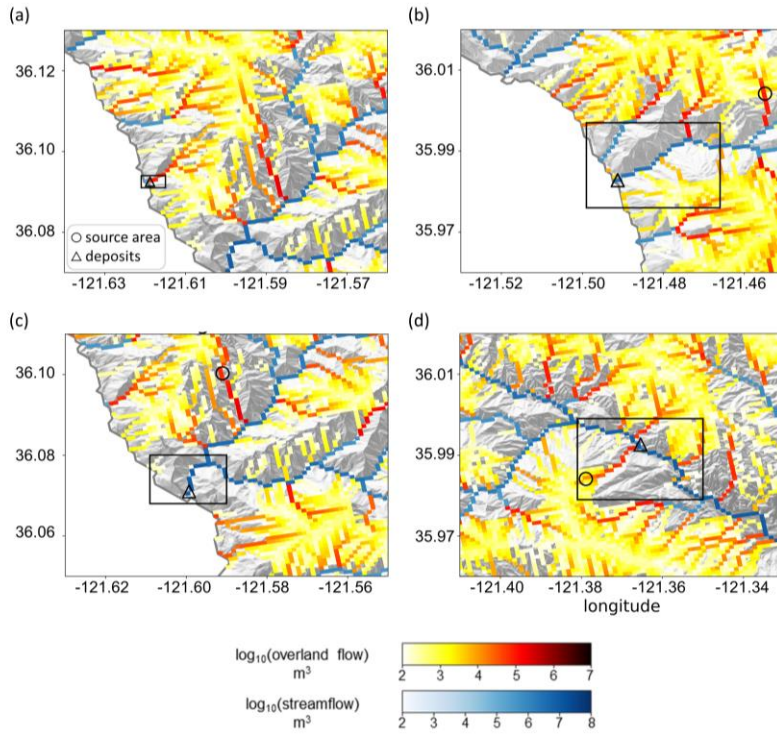
539 ~~We identified locations and extent of four debris flows from remote sensing data and field work~~
540 ~~(Fig. 3 & Fig. B1). rdNDVI shows vegetation loss caused by debris flows. Mill Creek, Big Creek,~~
541 ~~and Nacimiento were relatively large debris flows with runout lengths between 2–5 km. Rat~~
542 ~~Creek occurred deposits are located in a smaller catchment and had a runout length of ~300 m. The~~
543 ~~difference in runout length and debris flow size is primarily controlled by upstream catchment size.~~
544 ~~channels of 2nd Strahler stream order or above so they are simulated as channelized streamflow in~~
545 ~~our WRF-Hydro simulations. Due to its low stream order (1st Strahler stream order), Rat Creek is~~
546 ~~the only debris flow site modeled entirely as overland flow in our WRF-Hydro simulations.~~

547 At the four debris flow sites, we use three metrics to characterize hydrologic anomalies: (1)
548 accumulated runoff volume, (2) peak discharge, and (3) time to peak discharge. Fig. 7 depicts
549 accumulated channelized discharge volume (blue shading) and accumulated overland discharge
550 volume (yellow-red shading) from January 27th 00:00 to 28th 12:00 near the four debris flow sites
551 in the burn scar simulation. Accumulation time period is chosen such that it covers the first two
552 runoff surges in the simulated hydrographs which are likely associated with debris flows (Fig. 8)
553 given that nearly concurrent peak rainfall intensity and peak discharge is a signature characteristic
554 of debris flows (Kean et al., 2011). Runoff volume is on the order of 10⁴ m³ at Rat Creek and 10⁶
555 m³ at the other three sites.

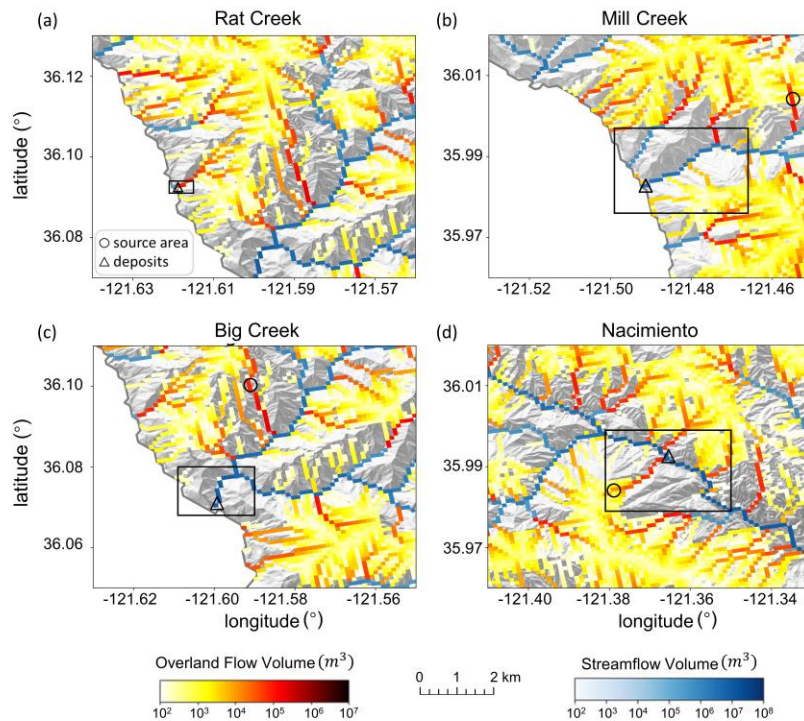
Formatted: Font: Bold, Font color: Black

Formatted: Space Before: 0 pt

Simulated overland flow and streamflow in burn scar simulation



Simulated overland flow and streamflow in burn scar simulation

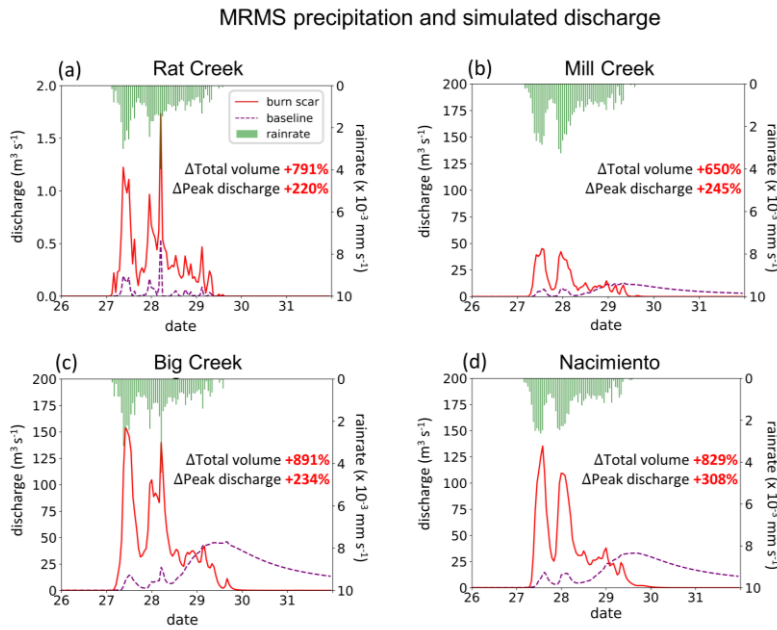


557
 558 **Fig. 7** WRF-Hydro simulated overland flow and streamflow in the burn scar simulation. (a)–(d)
 559 Total volume of accumulated overland flow (yellow-red shading) and streamflow (blue shading)
 560 ~~on log₁₀ scale~~ between January 27th 00:00 and 28th 12:00 at four debris flow sites draped over a
 561 hillshade of topography. Black rectangles correspond to domains in Fig. 3a–d. Black circles and
 562 triangles indicate debris flow source areas and deposits, respectively.

563
 564
 565 Dramatic hydrographic changes after inclusion of burn scar characteristics are simulated at debris
 566 flow source areas (Fig. B6 and Table B4) and deposition sites (Fig. 8 and Table 2). WRF-Hydro
 567 facilitates investigation of the hydrologic response at triggering and ~~deposition~~deposit locations
 568 and along the runout path. Here, to emphasize the high susceptibility downstream ~~hazards~~, our
 569 analysis is focused on debris flow deposits. At Rat Creek, where a section of CA1 collapsed, the
 570 magnitude of discharge substantially increases, and overland flow surges are concurrent with

571 rainfall bursts (Fig. 8a). Total discharge accumulated during the AR event increases approximately
 572 eight-fold (791%), and peak discharge more than triples compared to the baseline simulation (Fig.
 573 8a and Table 2). At Mill Creek, Big Creek, and Nacimiento, baseline hydrographs are characterized
 574 by less variability, muted responses to two early precipitation bursts, and a delayed third discharge
 575 peak that does not occur until ~3 days after AR passage (Fig. 8b–d). Maximum discharge peaks in
 576 the baseline hydrographs lag those in the burn scar simulation by ~2 days (Fig. 8b–d; Table 2). In
 577 the burn scar simulation, total volume substantially increases at the three channelized sites – total
 578 volume increases ~650% at Mill Creek, ~891% at Big Creek, and ~829% at Nacimiento (Fig. 8b–
 579 d and Table 2), and the absolute increase in volume is on the order of 10^6 m^3 (Table 2). Peak
 580 discharge more than triples at Mill Creek and Big Creek and more than quadruples at Nacimiento.
 581 Additionally, response times of the peak in discharge to the peak in precipitation decrease to less
 582 than an hour, highlighting the simulated flashiness of the burned catchments.

583
 584
 585



586
 587
 588 **Fig. 8|** WRF-Hydro simulated discharge time-series at four debris flow deposition locations. (a)–
 589 (d) MRMS precipitation (green bars) and simulated discharge time-series for January 26th 00:00

590 to 31st 23:00 at (a) Rat Creek, (b) Mill Creek, (c) Big Creek, and (d) Nacimiento deposition
 591 locations (black triangles in Fig. 7a–d) in baseline simulation (purple dashed line) and burn scar
 592 simulation (red line).

593
 594

595 *Table 2*

596 *The total runoff volume, peak discharge, and peak timing at debris-flow deposits*

Site name	Baseline simulation			Burn scar simulation			
	Total volume (m ³)	Peak discharge (m ³ s ⁻¹)	Highest peak timing	Total volume (m ³)	Peak discharge (m ³ s ⁻¹)	1 st Peak timing	2 nd Peak timing
Rat Creek	6,897	0.54	28 th 05:00	61,425 (+791%)	1.73 (+220%)	27 th 09:00	28 th 05:00
Mill Creek	312,925	13.10	29 th 08:00	2,347,457 (+650%)	45.21 (+245%)	27 th 13:00	27 th 23:00
Big Creek	842,808	46.10	29 th 16:00	8,354,095 (+891%)	154.10 (+234%)	27 th 10:00	28 th 05:00
Nacimiento	743,531	33.15	29 th 16:00	6,904,706 (+829%)	135.41 (+308%)	27 th 14:00	28 th 00:00

597 **Table 2** | The total runoff volume, peak discharge, and peak timing in the baseline and burn scar
 598 simulations from January 27th 00:00 to 31st 23:00 at deposition sites of Rat Creek, Mill Creek, Big
 599 Creek, and Nacimiento debris flows (black triangles in Fig. 7a–d). The peak timing shown in the
 600 baseline simulation is for the highest peak. The percent change of the total volume and peak
 601 discharge in the burn scar simulation relative to the baseline simulation are shown in parentheses.
 602

603
 604

605 **5.3 Debris flow ~~hazard~~susceptibility assessment for the Dolan burn scar**

606 Since high magnitude runoff is often the cause and precursor of runoff-generated debris flows in
 607 burned areas (Cannon et al., 2003, 2008; Rengers et al., 2016), we use simulated accumulated
 608 volume of overland flow and streamflow to assess runoff-generated debris flow ~~hazard~~
 609 ~~potential~~susceptibility under pre-fire (i.e., baseline; Fig. 9a&d) and postfire (i.e., burn scar
 610 simulation; Fig. 9b&e) conditions. We assess changes at both stream and catchment levels and use
 611 the difference between burn scar and baseline simulations to assess added debris flow ~~hazard~~
 612 ~~potential~~susceptibility (Fig. 9c&f). Consistent with the increasing erosive and entrainment power
 613 associated with increasing discharge, our debris flow ~~hazard~~susceptibility increases as the
 614 accumulated discharge volume increases. To reduce the effects of catchment size on the volume-
 615 based ~~hazard~~susceptibility levels, we normalize a catchment’s discharge volume by the area of the

616 catchment (Santi ~~et al., 2012~~ & Morandi, 2013; Fig. 9d–f). Non-normalized catchment
617 ~~hazard~~susceptibility maps are also provided (Fig. B7).

618
619 In the pre-fire baseline simulation, the AR-induced precipitation produces lower debris flow
620 ~~hazard~~susceptibility over most of the domain, but elevated ~~hazard~~susceptibility along stream
621 channels (Fig. 9a). We note no substantial differences between areas in or out of the burn scar. In
622 the burn scar simulation, debris flow ~~hazard~~susceptibility levels increase across the Dolan burn
623 scar and along channels outside but downstream of the burn scar (Fig. 9b–c). The discharge volume
624 increases by an order of magnitude near Rat Creek, Big Creek, Mill Creek, and Nacimiento. Within
625 the burn scar, ~~hazard~~susceptibility along major stream channels, such as the Nacimiento River
626 and San Antonio River increase. Outside the burn scar, ~~hazard~~susceptibility levels along river
627 channels downstream of the burn scar, such as the Arroyo Seco River, also increase (Fig. 9c).

628
629 At the catchment level, debris flow ~~hazard~~susceptibility is assessed using accumulated
630 discharge volumes normalized by catchment areas (Fig. 9d–f). Accumulated discharge volumes
631 are ~~assessed~~calculated at the outlet of each catchment between January 27th 00:00 to 28th 12:00.
632 ~~The catchment-area normalized volume is then used as the susceptibility index and is classified~~
633 ~~into five categories based on equal intervals on log₁₀ scale. The susceptibility categorization~~
634 ~~follows: “very low” (~10³ m³ km⁻²), “low” (~10⁴ m³ km⁻²), “medium” (~10⁵ m³ km⁻²), “high” (~10⁶~~
635 ~~m³ km⁻²), and “very high” (~10⁷ m³ km⁻²). In the baseline simulation, the majority of catchments~~
636 ~~are subject to relatively low or very low debris flow hazard compared to the burn scar~~
637 ~~simulations~~susceptibility with total normalized discharge volume less than ~~10³10⁴~~ m³ km⁻² (Fig. 9d).
638 In the burn scar simulation, ~~over about~~ half of ~~the~~ catchments within the Dolan burn scar have
639 ~~normalized discharge volume greater than 10⁵ m³ km⁻², while over medium susceptibility or above.~~
640 ~~and about~~ 1/4 of basins ~~reach 10⁶ m³ km⁻² are subject to high debris flow susceptibility~~ (Fig. 9e).
641 The additional debris flow ~~hazard~~susceptibility brought about by the inclusion of wildfire burn
642 scar characteristics is substantial (Fig. 9f).

643 To summarize changes in debris flow ~~hazard~~susceptibility as a result of including burn scar
644 characteristics in WRF-Hydro simulations, we create distributions of pre-fire baseline and burn
645 scar catchment-area normalized discharge from the 404 catchments located within the Dolan burn
646 scar perimeter (Fig. 10). After incorporating burn scar characteristics, the full distribution shifts to
647 the right, indicating increased ~~hazard~~susceptibility levels – a shift considered robust by a Student’s
648 t-test (p value: 4.6E-45). A quantitative assessment of this shift indicates that the mean catchment
649 area normalized discharge volume increases by ~1300% (~~from 380k to 5.5M m³ km⁻²~~) while the
650 standard deviation increases ~1400% (~~from 1.6M to 23.0M m³ km⁻²~~), (Table 3). We also assess
651 shifts at a range of distribution percentiles: 5P: 148% (~~0.6k to 1.5k m³ km⁻²~~),%, 25P: 725%
652 (~~3.7k to 30.7k m³ km⁻²~~),%, 50P: 924% (~~13k to 135k m³ km⁻²~~),%, 75P: 980% (~~120k to 1.3M~~
653 ~~m³ km⁻²~~),%, and 95P: 1300% (~~2.1M to 29.1M m³ km⁻²~~), (Table 3). In the burn scar simulation,
654 ~~more than nearly~~ half of catchments have normalized volumes > 10⁵ m³ km⁻² ~~and more than (i.e.,~~
655 ~~medium susceptibility) and about~~ 1/4 of catchments have volumes > 10⁶ m³ km⁻² ~~(i.e., high~~

656 susceptibility) – values that correspond to the 75P and 90P of the baseline simulation, respectively.
 657 Disproportionate shifting of the right tail of the distribution suggests that extreme debris flow
 658 ~~hazards increases~~susceptibility increases non-linearly under simulated burn scar conditions.

Formatted: Font color: Black

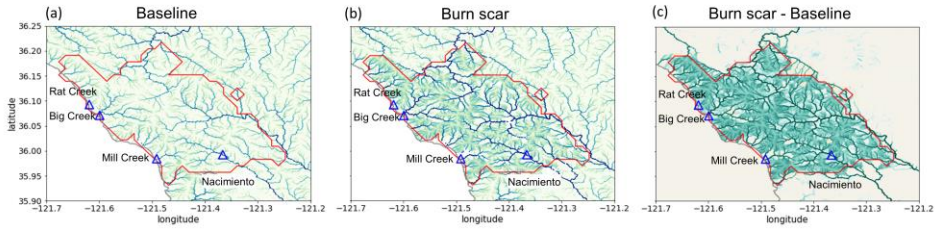
659 Table 3
 660 Statistics of catchment area-normalized discharge volume in baseline and burn scar simulations

	<u>mean</u>	<u>std</u>	<u>5P</u>	<u>25P</u>	<u>50P</u>	<u>75P</u>	<u>95P</u>
<u>Baseline simulation</u> (m ³ km ⁻²)	<u>380k</u>	<u>± 1.6M</u>	<u>0.6k</u>	<u>3.7k</u>	<u>13k</u>	<u>120k</u>	<u>2.1M</u>
<u>Burn scar simulation</u> (m ³ km ⁻²)	<u>5.5M</u>	<u>± 23.0M</u>	<u>1.5k</u>	<u>30.7k</u>	<u>135k</u>	<u>1.3M</u>	<u>29.1M</u>
<u>Relative percent change</u>	<u>1300%</u>	<u>1400%</u>	<u>148%</u>	<u>725%</u>	<u>924%</u>	<u>980%</u>	<u>1300%</u>

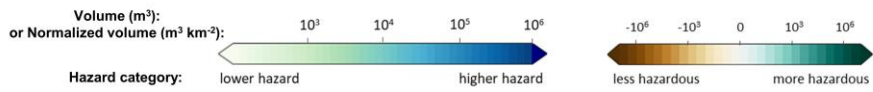
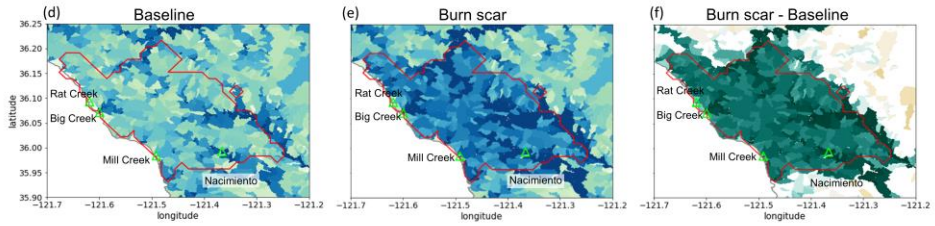
661 Table 3 | Statistics, including the mean, standard deviation (std), 5P, 25P, 50P, 75P, and 95P, of
 662 the catchment-area normalized discharge volume for all basins within the Dolan burn scar in the
 663 baseline and burn scar simulation and their relative percent changes.

665 Our catchment-area normalized discharge volume-based ~~hazard~~susceptibility assessment also
 666 indicates that the catchments containing Mill Creek, Big Creek, and Nacimiento ~~had elevated~~
 667 ~~hazard potential~~have high or very high susceptibility (Fig. 9d–f), consistent with our (limited)
 668 debris flow observations. Other areas with elevated ~~hazard~~susceptibility include catchments
 669 containing the Arroyo Seco and San Antonio Rivers. Beyond the burn scar perimeter, effects of
 670 fire expand to adjacent and downstream catchments, and ~~the some~~ drainage basins ~~of along~~
 671 Arroyo Seco and Nacimiento Rivers are simulated to have ~~potentially hazardous conditions~~very
 672 high susceptibility, i.e., normalized discharge volumes in excess of ~~10⁶~~10⁷ m³ km⁻² (Fig. 9e&f).
 673

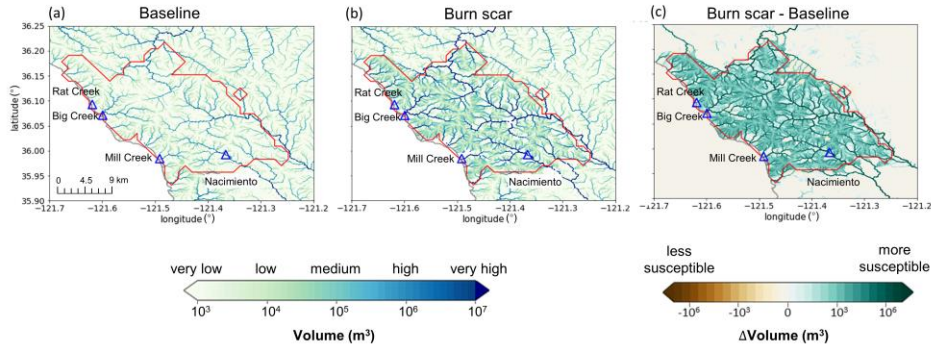
Stream channel hazard assessment



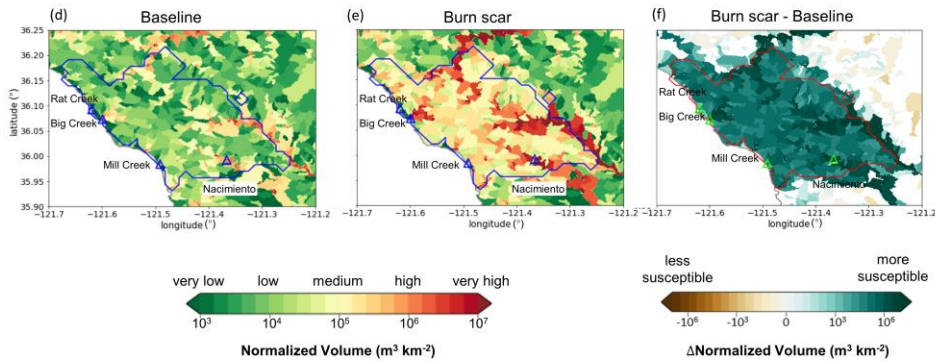
Normalized catchment hazard assessment



Postfire Debris Flow Susceptibility



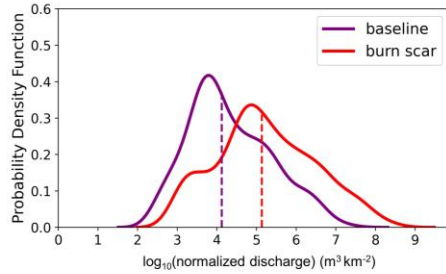
Catchment-area Normalized Postfire Debris Flow Susceptibility



675
 676
 677 **Fig. 9|** Discharge volume-based runoff-generated postfire debris flow hazards susceptibility.
 678 Debris flow hazards susceptibility at individual stream level for the (a) baseline, (b) burn scar, and
 679 (c) difference between burn scar and baseline simulations. Hazard Susceptibility is estimated as
 680 total discharge volume from January 27th 00:00 to 28th 12:00. (d)–(f) Normalized debris flow
 681 hazards susceptibility by catchment area at catchment level. For each catchment, the
 682 hazards susceptibility is determined by total discharge volume at the catchment outlet from January
 683 27th 00:00 to 28th 12:00 divided by catchment area.

Formatted: Superscript

Formatted: Superscript



684

685 **Fig. 10** Distributions of accumulated discharge volumes at the outlet of the 404 catchments
 686 normalized by upstream catchment areas within Dolan burn scar in the baseline simulation (purple
 687 line) and in the burn scar simulation (red line). Dashed vertical lines indicate median values.

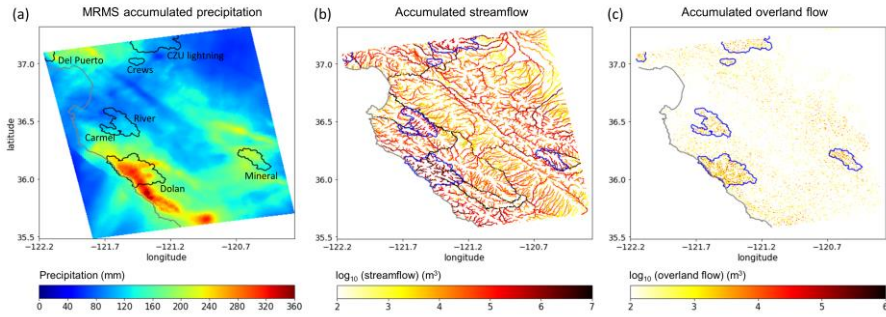
Formatted: Space After: 12 pt, Don't keep with next

688

5.4 Debris flow hazard assessment at regional scales

689 While the results we present above primarily focus on hazards in the Dolan burn scar, our WRF-
 690 Hydro domain includes a number of additional 2020 wildfire burn scar sites (Fig. 1a). Given the
 691 long filament-like structure of western U.S. landfalling ARs, the heterogeneous nature of
 692 landfalling trajectories, and the potential for systems to interact with diverse topographic terrains,
 693 the development of tools capable of regional hazard assessments under high gradient precipitation
 694 events is crucial—particularly in a wildfire-prone region like California. To demonstrate the
 695 potential utility of WRF Hydro in regional applications, we assess hazards over our full domain
 696 (Fig. 11). We find that hazard potential, from both channelized and overland flows, is greatest
 697 within the burn scar sites, with maximum hazards found in the Dolan burn scar, consistent with
 698 the location of elevated precipitation along the Coast Ranges—where more than 300 mm of rain
 699 fell over three days (Fig. 11). Other high hazard-elevated precipitation regions within our domain
 700 include the western edge of the Sierra Nevada and areas north of Monterey Bay, which collocate
 701 with the Mineral and Del Puerto burn scars, respectively. Similar to our Dolan burn scar focused
 702 analysis, areas within and downstream of these burn scar sites have elevated streamflow discharge
 703 volumes compared to the non-burned areas (Fig. 11b). Likewise, areas of heightened accumulated

704 ~~overland flow are elevated in burn-scar regions, but also demonstrate a strong correspondence to~~
 705 ~~the spatial distribution of precipitation (Fig. 11a & c).~~



706
 707 ~~Fig. 11| MRMS accumulated precipitation and regional debris flow hazard assessment. (a) MRMS~~
 708 ~~accumulated precipitation during January 27th 00:00 to 29th 23:00 over the model domain (shading,~~
 709 ~~mm). Names of burn scars are labeled in black. (b) Accumulated streamflow (yellow to red~~
 710 ~~shading; m^3) and (c) accumulated overland flow from 27th 00:00 to 28th 12:00 over the model~~
 711 ~~domain (yellow to red shading; m^3). Wildfire perimeters of 2020 wildfire season are outlined in~~
 712 ~~black in (a), and in blue in (b) and (c). The coastline of California is in grey.~~

Formatted: Superscript
 Formatted: Superscript
 Formatted: Superscript
 Formatted: Superscript

713

714 **6 Discussion**

715 Given the historic and growing frequency of wildfires in the western U.S. (Swain 2021; Williams
 716 et al., 2019; Goss et al., 2020; Swain 2021) and globally (Jolly et al., 2015; Flannigan et al., 2013;
 717 Jolly et al., 2015), developing tools to investigate, better understand, and potentially predict
 718 changes in burn scar hydrology and natural hazards at regional scales is critical. Here, we
 719 demonstrate the first use of WRF-Hydro to simulate the ~~surface hydrologic response~~
 720 ~~oversusceptibility of~~ a burn scar ~~to postfire debris flows~~ during a landfalling AR. We augmented
 721 the default version of WRF-Hydro to output overland flow and to replicate burn scar behavior by
 722 adjusting vegetation type and infiltration rate parameters. WRF-Hydro simulations were validated
 723 against PSL soil moisture and USGS streamflow observations before we used simulated
 724 streamflow and overland flow volumes to characterize debris flow ~~hazard potential~~.

725
 726 ~~susceptibility.~~ A comparison between baseline and burn scar simulations demonstrated that
 727 changes in hydraulic properties of burned areas causes drastic changes in surface flows, including
 728 faster discharge response times, ~~greater discharge volumes, and overall flashier hydrologic~~
 729 ~~behavior in surface flows.~~ As a result of including bur-scar characteristics in WRF-Hydro

730 ~~simulations, median catchment area normalized discharge volume increases nine fold, while 95P~~
731 ~~volume increases 13 fold. The magnitude of our simulated changes is and greater peak discharge~~
732 ~~and total volumes,~~ consistent with findings from previous postfire hydrology studies (Anderson et
733 al., 1976; Scott, 1993; Meixner & Wohlgemuth, 2003; [Kean et al., 2011](#); Kinoshita & Hogue, 2015;
734 ~~Kean~~[Brunkal & Santi, 2016](#); [Williams et al., 2011](#)~~2022~~). At ~~Rat Creek, where a debris flow~~
735 ~~destroyed CA1, our model simulation predicted an eight~~the catchment level, for the 404
736 ~~catchments located within the Dolan burn scar, median catchment area-normalized volume~~
737 ~~increases nine-fold~~ increase in accumulated overland flow and a tripling in peak discharge when
738 ~~compared~~relative to the baseline ~~simulation.~~ At. In addition, Mill Creek, Big Creek, and
739 Nacimiento, the increase of runoff volume from the baseline to the burn scar simulation is on the
740 order of 10^6 m^3 . Our hazard assessments based on catchment area normalized discharge volumes
741 indicated that Mill Creek, Big Creek, and Nacimiento were under elevated debris flow hazards
742 ~~basins were simulated to have high-to-very high debris flow susceptibility,~~ corresponding well
743 with identified debris flow occurrences.

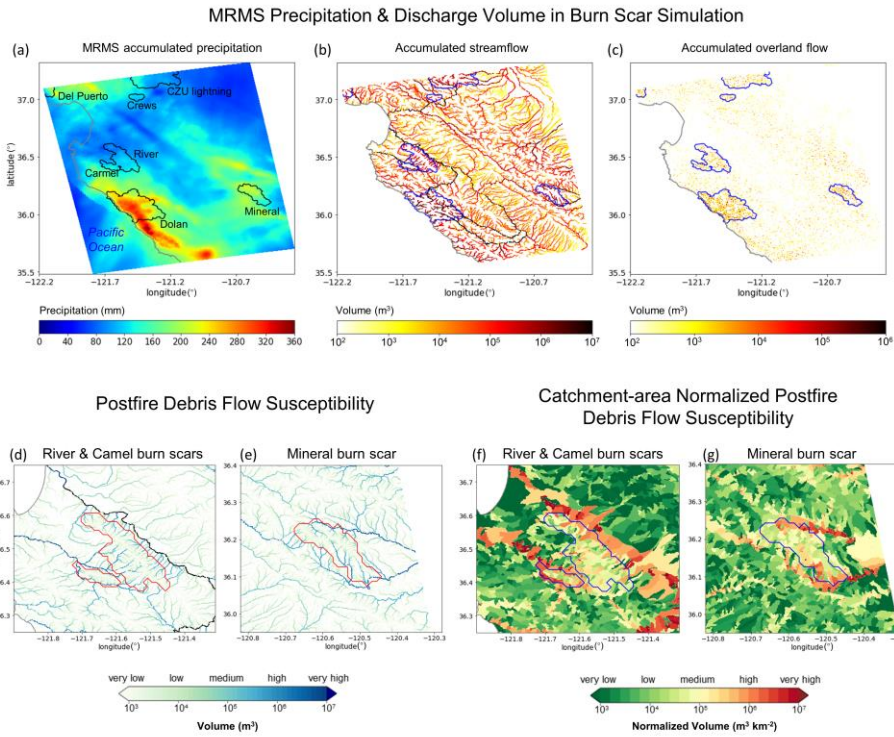
744
745 Despite methodological differences, our debris flow ~~hazard assessment~~susceptibility map for this
746 AR event is generally consistent with the USGS' postfire, pre-AR, design-storm-based preliminary
747 hazard assessment (USGS, 2020). As described above, USGS preliminary hazard assessments use
748 logistic regression models to estimate the likelihood of debris flow occurrence and multivariate
749 linear regression models to estimate debris flow volumes. ~~This~~The USGS empirical approach is
750 trained on historical western U.S. debris flow occurrence and magnitude data and incorporates
751 ~~estimated~~burn scar soil erodibility and burn severity data (Cannon et al., 2010; Gartner et al., 2014;
752 Staley et al., 2016). For precipitation, the USGS assessment utilizes a design storm approach that
753 assumes 1–5 year return interval magnitude precipitation falls uniformly over a region/burn scar
754 (USGS, 2020). For the Dolan burn scar, both assessments find that large stream channels had
755 relatively higher ~~hazard levels~~susceptibility than small streams or overland areas. However, a close
756 comparison of ~~hazard~~the two maps reveals differences in spatial distribution of high-
757 ~~hazard~~hazardous catchments. In the USGS assessment, higher ~~hazard levels are~~likelihood is
758 predicted north and southeast of the burn scar, whereas in our assessment the highest hazards
759 ~~occur~~susceptibility occurs along major stream channels. We hypothesize that USGS-assessed
760 areas of higher hazard potential are related to their use of [spatially uniform](#) design-storm
761 precipitation (see Fig. 2 for MRMS precipitation footprint) and burn severity data (Burned Area
762 Emergency Response, 2020).

763
764 Comparison with the USGS [hazard](#) assessment framework suggests room for improvement in
765 WRF-Hydro-based assessments (i.e., inclusion of burn severity and soil erodibility data), but also
766 highlights the potential utility of working with spatially-distributed and time-varying precipitation.
767 However, this also means the accuracy of WRF-Hydro predictions depends on the accuracy of
768 precipitation forcing, and in our hindcast application, MRMS precipitation data (Appendix A).
769 Accordingly, our WRF-Hydro-based ~~hazard~~ assessment could benefit from precipitation products

770 mosaiced from various sources to constrain precipitation-based uncertainties (e.g., gauge-
771 corrected and/or Mountain Mapper MRMS), although the long processing time of these datasets
772 inhibits timely post-event assessments.

773 In addition to the above results focused primarily on the Dolan burn scar, a key feature of WRF-
774 Hydro is its ability to simulate the land surface hydrology of expansive geographic domains, e.g.,
775 NOAA runs the National Water Model over the entire continental U.S. Development of tools
776 capable of regional susceptibility assessments is crucial, particularly in a wildfire-prone region
777 like California, due to the large spatial scale, diverse morphology, and often tight spatial gradients
778 of precipitation events and their interactions with geographically widespread wildfire burn scars.
779 For example, landfalling ARs are often long (1000s of km) filament-like systems with
780 heterogeneous intensity gradients along their length. As a demonstration of wide geographic
781 applicability, we assess susceptibility over our full model domain which includes more than 10,000
782 catchments and a number of 2020 wildfire burn scars in addition to the Dolan burn scar (Fig 11).
783 The domain-wide analysis reveals elevated discharge volume, i.e., elevated susceptibility, in areas
784 of high precipitation and in burned terrains (Figs. 11a–c). We highlight channelized and
785 catchment-area normalized debris flow susceptibility in non-Dolan burn scar sites in Figs. 11d–g.
786 In an operational forecast context, the ability to simulate landslide and debris flow susceptibilities
787 and hazards over numerous catchments at meteorologically appropriate scales represents a step-
788 change in the field. We argue that our demonstration of WRF-Hydro’s debris flow susceptibility

789 hindcast capabilities should motivate further exploration and development for potential use in
 790 operational hazard forecasting.



791

792 **Fig.**

793 As a water-only model, WRF-Hydro is currently restricted to simulating the hydrologic ingredients
 794 of debris flows.11| MRMS accumulated precipitation and discharge volume informed regional
 795 debris flow susceptibility. (a) MRMS accumulated precipitation during January 27th 00:00 to 29th
 796 23:00 over the model domain (shading; mm). Names of burn scars are labeled in black. (b)
 797 Accumulated streamflow (yellow-to-red shading; m³) and (c) accumulated overland flow from 27th
 798 00:00 to 28th 12:00 over the model domain (yellow-to-red shading; m³). (d)–(e) Stream-level
 799 postfire debris flow susceptibility as Fig. 9b but for River and Camel burn scars. (f)–(g)
 800 Catchment-area normalized debris flow susceptibility as Fig. 9e but for River and Camel burn
 801 scars. Wildfire perimeters of 2020 wildfire season are outlined in black in (a), in blue in (b), (c),
 802 (f), and (g), and in red in (d) and (e). The coastline of California is depicted in grey.

803

Formatted: Font: Bold, Font color: Black

Formatted: Superscript

Formatted: Superscript

Formatted: Superscript

Formatted: Superscript

804 In addition to investigating the operationalization of WRF-Hydro's natural hazard prediction
805 capabilities, we note that our susceptibility-focused methodology could be advanced to hazard
806 assessment, in line with current USGS products. The USGS Emergency Assessment of Postfire
807 Debris-flow Hazard predicts debris flow volume and likelihood. To advance from susceptibility to
808 hazard assessment, our methodology would need to incorporate both debris flow volume estimates
809 and occurrence likelihoods. In the following, we highlight research directions that could help
810 advance our susceptibility-focused methodological framework. WRF-Hydro is a water-only model.

811 While water-only models have been widely used to investigate and better understand debris flow
812 dynamics (Arattano & Savage, 1994; Tognacca et al., 2000; Arattano & Franzi, 2010; Rengers et
813 al., 2016; McGuire & Youberg, 2020; Di Cristo et al., 2021), sediment supply, soil erodibility, and
814 other sedimentological factors ~~also~~ play important roles in determining the potential for and
815 severity of mass failure events (McGuire et al., 2017). Developing a runoff-generated debris flow
816 model that couples hydrologic and sediment erosion and transport processes ~~would represent a~~
817 ~~significant advance and be of great practical use (Banihabib could help to characterize postfire~~
818 ~~debris flow volumes. Indeed, previous efforts have demonstrated the capacity to couple WRF-~~
819 ~~Hydro with sediment flux models (Yin et al., 2020; Shen et al., 2021). At a minimum, soil grain~~
820 ~~size maps and domain specific rainfall intensity duration curves~~In addition to sediments, burn scar
821 ash can provide guidance to define transitions from water floods to debris flows if
822 historicalcomprise a substantial fraction of the total debris flow data is available in the study
823 domain (McGuire & Youberg, 2020; volume (e.g., Reneau et al., 2007). As such, efforts to
824 constrain ash availability and entrainment in hydrologic flows could prove fortuitous in hazard
825 assessment and prediction efforts. If WRF-Hydro is not coupled with sediment models, a domain-
826 specific rainfall ID threshold trained with historic landslide inventory and triggering rainfall events
827 (Tognacca et al., 2000; Gregoretti & Dalla Fontana, 2007, 2008; Cannon et al., 2007.) or a newly
828 developed dimensionless discharge and Shields stress threshold (Tang et al., 2019; McGuire &
829 Youberg, 2020) could provide guidance to help identify debris flow triggering time and location,
830 which in turn may improve WRF-Hydro's debris flow initiation identification.

831
832
833 In addition to constraining potential postfire debris flow volumes, WRF-Hydro's application in
834 debris flow studies could be advanced via concerted engagement with uncertainties that are both
835 external (meteorological forcing data) and internal (physical parameters) to the model. Previous
836 studies have demonstrated that precipitation is often the largest source of uncertainty in hydrologic
837 predictive models (Hapuarachchi et al., 2011; Alfieri et al., 2012). Engagement with precipitation
838 forcing uncertainties in past, near-term, and future contexts could provide probabilistic nuance to
839 natural hazard investigations. For example, (a) debris flow hindcast studies could use a diversity
840 of precipitation datasets to isolate precipitation-derived debris flow uncertainties in historic events,
841 (b) operational forecast efforts could utilize ensemble-based weather forecast data to inform
842 likelihood statements in debris flow hazard assessments, and (c) probabilistic projections of debris
843 flow likelihood in future climates could assess and partition uncertainties derived from emission

844 pathway, model structure, or internal variability effects on meteorological forcings (Nikolopoulos
845 et al., 2019; Hawkins & Sutton, 2009; Deser et al., 2020). Uncertainties internal to WRF-Hydro
846 are also ripe for investigation. Probabilistic predictions crafted from an ensemble of perturbed
847 model physics simulations have been used to predict rainfall-triggered shallow landslides (Raia et
848 al., 2014; Canli et al., 2018; Zhang et al., 2018). Similar efforts using WRF-Hydro could target
849 post-wildfire debris flows.

850
851
852 Lastly, the above discussion of potential WRF-Hydro applications and advancements speaks to the
853 adaptability and customization of this open-source numerical model. An additional layer of WRF-
854 Hydro’s adaptability concerns its geographic focus. While we calibrate and use the model over a
855 central California domain, the choice of geographic footprint is only limited by the availability of
856 requisite initial and boundary conditions, environmental observations for calibration, and
857 computational resources. For use in non-central California domains, we recommend calibration
858 beginning with the default version of the model. Given the ecological and geological diversity of
859 locations that experience wildfires and debris flows, it is likely that calibrations distinct from those
860 reported here will be needed in different regions. For example, soil sealing effects, infiltration, and
861 runoff in wetter and more vegetated locations, such as Oregon, USA, behave differently than those
862 in central California (Palmer, 2022). As such, calibration of relevant model parameters (e.g.,
863 saturated hydraulic conductivities) should be based on a physics-informed approach that accounts
864 for local environmental conditions and hydrologic behaviors. Indeed, given the ability to simulate
865 large heterogeneous geographic domains, it is likely that different regions within a given domain
866 may require different calibration schemes. As WRF-Hydro is fully distributed, spatially
867 heterogeneous calibrations are non-problematic. This spatial adaptability may prove particularly
868 helpful in post-wildfire debris flow hazard assessments when considering multiple generations of
869 wildfires and variable degrees of burn scar severity and recovery.

870 **7 Conclusion**

871
872 Use of Here we augment WRF-Hydro to simulate runoff-generated assess regional postfire debris
873 flow hazards insusceptibility. Our methodology involves output of simulated overland flow data
874 and alteration of the model’s representation of burn scar settings represents a novel application. It
875 is notable that inscars. In this application we have balanced the computational cost of a regional
876 domain with our choice of resolved spatial resolution for terrain routing and overland flow
877 calculations (100 m). However, WRF-Hydro has previously been applied to smaller domains at
878 higher terrain routing resolutions (~30 m). Future work could assess the use of the model to study
879 burn scar hydrology at finer spatial scales, should the application warrant and should underlying
880 data at sufficient resolution exist. Other potential applications of our ~~modified~~augmented model
881 framework include alpine areas and steep hillslopes with sparse vegetation where runoff-generated
882 debris flows dominate over landslide-initiated ones (Davies et al., 1992; Coe et al., 2003, 2008).

883
884 ~~Further~~Furthermore, our burn scar parameter changes are performed to Noah-MP, which is the
885 core land surface component of the ~~National Centers for Environmental Prediction~~NCEP Global
886 Forecast System (GFS) and Climate Forecast System (CFS), thus the findings presented herein,
887 are likely to prove useful in the broader worlds of forecast meteorology and climate science. In
888 addition, here WRF-Hydro is driven by historical precipitation and meteorological data, i.e., in
889 hindcast mode. ~~We see no reason why~~However, this modeling framework could ~~not~~ also be
890 employed to project hazards under future climatic conditions (e.g., Huang et al., 2020), or given
891 its relatively low computational expense, in operational forecast mode. Indeed, modern ensemble-
892 based meteorological forecasting could provide high spatiotemporal forcing data with which
893 disaster preparedness managers could probabilistically assess debris flow hazard potential, and
894 issue advanced life and property saving warnings.

895
896
897

Formatted: Left, Line spacing: single

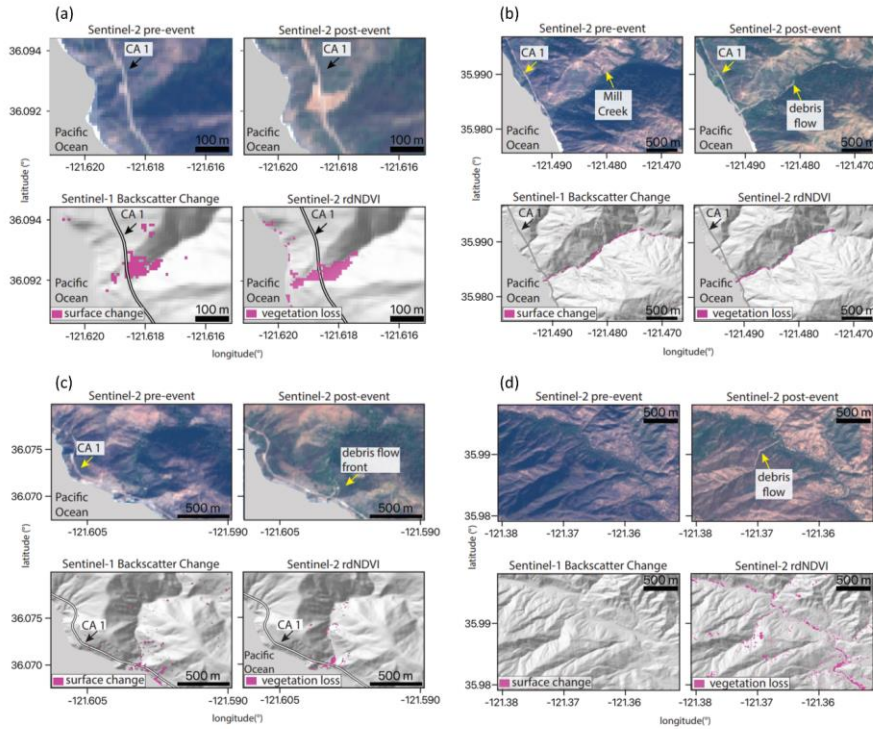
898 **Appendix A**

899 **Text A1. Multi-Radar/Multi-Sensor System (MRMS) radar-only precipitation estimate and**
900 **uncertainty**

901 MRMS is a precipitation product that covers the contiguous United States (CONUS) on 1-km grids.
902 It combines precipitation estimates from sensors and observational networks (Zhang et al.,
903 2011, 2014, 2016), and is produced at the National Centers for Environmental Prediction (NCEP)
904 and distributed to National Weather Service forecast offices and other agencies. Input datasets
905 used to produce MRMS include the U.S. Weather Surveillance Radar-1988 Doppler (WSR-88D)
906 network and Canadian radar network, Parameter-elevation Regressions on Independent Slopes
907 Model (PRISM; Daly et al. 1994, 2017), Hydrometeorological Automated Data System (HADS)
908 gauge data with quality control (Qi et al., 2016), and outputs from numerical weather prediction
909 models. There are four different MRMS quantitative precipitation estimates (QPE) products
910 incorporating different input data or combinations: radar only, gauge only, gauge-adjusted radar,
911 and Mountain Mapper. For our study period (i.e., January 1–31, 2021), only the radar-only QPE
912 is currently available.

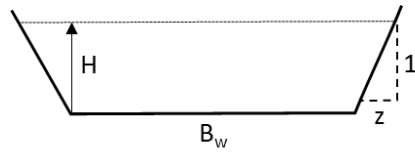
913
914 We acknowledge that precipitation data has uncertainties. Use of different precipitation products
915 may produce different results. A study comparing different gridded precipitation datasets including
916 satellite-based precipitation data, gauge dataset, and multi-sensor products revealed large
917 uncertainties in precipitation intensity (Bytheway et al., 2020). However, comparing different
918 precipitation datasets to characterize uncertainties is beyond the scope of this study. MRMS
919 provides gridded precipitation at high temporal (hourly) and spatial (1-km) resolutions, making it
920 a useful tool to demonstrate the utility of WRF-Hydro in post-wildfire debris flow
921 [hazard susceptibility](#) assessments.

922 **Appendix B**



923
 924
 925 **Fig. B1** Optical- and SAR-based remote sensing data of four debris flows. Optical data from
 926 Sentinel-2 show pre- and post-debris flow imagery in real color. rdNDVI calculated from the
 927 Sentinel-2 data show a decrease in vegetation corresponding to debris flow locations. Sentinel-1
 928 backscatter change shows the change in ground surface properties determined by calculating the
 929 log ratio of pre- and post-event SAR images. The pre-event, post-event satellite images, Sentinel-
 930 1 Backscatter, and Sentinel-2 rdNDVI change at (a) Rat Creek, (b) Mill Creek, (c) Big Creek, and
 931 (d) Nacimiento.

932
 933
 934



935
936 **Fig. B2** Schematic trapezoidal shape and related parameters of channels in WRF-Hydro. B_w is
937 the channel bottom width (m), z is the channel side slope (m), and H is water elevation (m). The
938 cross-sectional area of flow is calculated as $(B_w + H z)H$.

939

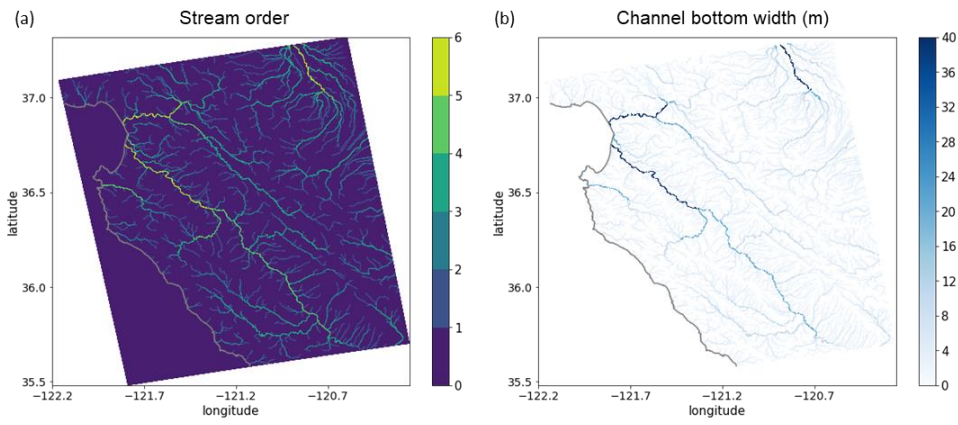
940 **Table B1** Parameters of trapezoidal channels in WRF-Hydro.

Stream order	Channel bottom width B_w (m)	Channel side slope z (m)	Manning's roughness coefficient n
1	1.5	3	0.33
2	3	1	0.21
3	5	0.5	0.09
4	10	0.18	0.06
5	20	0.05	0.04
6	40	0.05	0.03
7	60	0.05	0.02
8	70	0.05	0.02
9	80	0.05	0.01
10	100	0.05	0.01

941
942 **Table B1** Parameters of the trapezoidal channels in WRF-Hydro including channel bottom width
943 B_w (m), channel side slope z (m), and Manning's roughness coefficient n .

944

945



946

947 **Fig. B3** (a) Stream order defined by the USGS 30-m DEM in our WRF-Hydro model domain
 948 and (b) the channel bottom width (m) which is a function of stream order (Table B1).

949

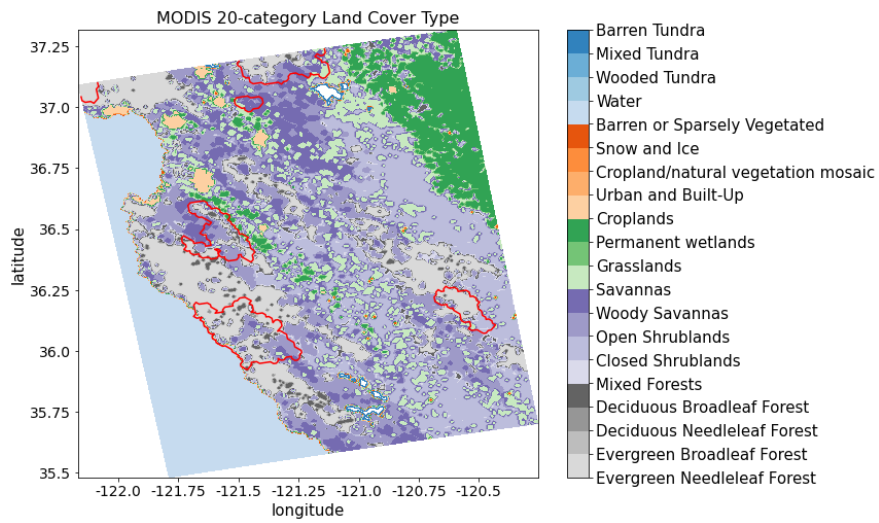
950 *Table B2*

951 *MODIS IGBP 20-category land cover type and properties in Noah-MP LSM*

Land cover code	Land cover type	Canopy height (m)	Max carboxylation rate at 25°C ($\mu\text{mol CO}_2/(\text{m}^2 \cdot \text{s})$)	Overland flow roughness
1	Evergreen Needleleaf Forest	20	50	0.2
2	Evergreen Broadleaf Forest	20	60	0.2
3	Deciduous Needleleaf Forest	18	60	0.2
4	Deciduous Broadleaf Forest	16	60	0.2
5	Mixed Forests	16	55	0.2
6	Closed Shrublands	1.1	40	0.055
7	Open Shrublands	1.1	40	0.055
8	Woody Savannas	13	40	0.055
9	Savannas	10	40	0.055
10	Grasslands	1	40	0.055
11	Permanent wetlands	5	50	0.07
12	Croplands	2	80	0.035
13	Urban and Built-Up	15	0	0.025
14	Cropland/natural vegetation mosaic	1.5	60	0.035
15	Snow and Ice	0	0	0.01
16	Barren or Sparsely Vegetated	0	0	0.035
17	Water	0	0	0.005
18	Wooded Tundra	4	50	0.055
19	Mixed Tundra	2	50	0.055
20	Barren Tundra	0.5	50	0.055

952 **Table B2** MODIS IGBP 20-category land cover type and properties in Noah-MP LSM.

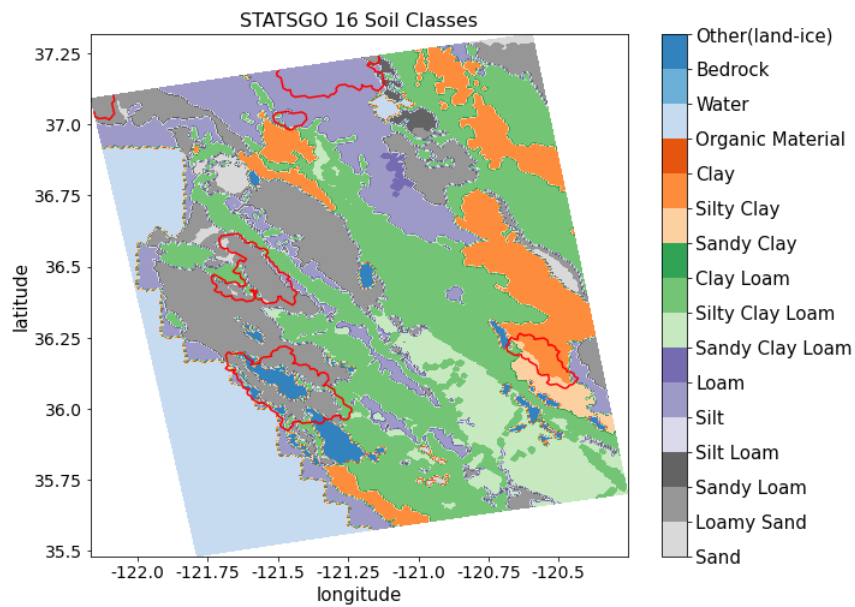
953
954
955



956 **Fig. B4** MODIS IGBP 20-category land cover type in the model domain. Red polylines are 2020
 957 wildfire burn scar perimeters.

958

959



960 **Fig. B5** 1-km STATSGO data with 16 soil texture types. Red polylines are 2020 wildfire burn
 961 scar perimeters.

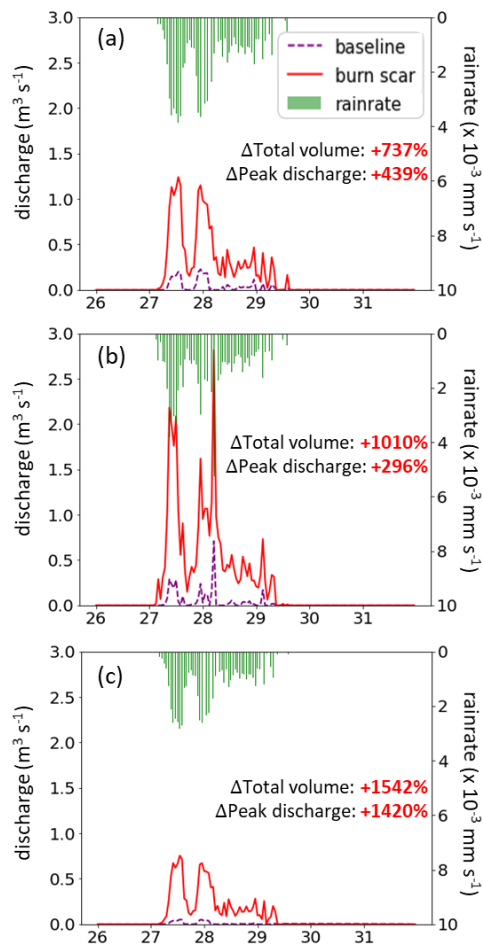
962
 963
 964
 965
 966

967 *Table B3*
 968 *Default and calibrated soil parameters in WRF-Hydro*
 969

Soil type	Default			After calibration		
	Grain size distribution index	Porosity	Saturated hydraulic conductivity (m s ⁻¹)	Grain size distribution index	Porosity	Saturated hydraulic conductivity (m s ⁻¹)
Sand	2.79	0.339	4.66E-5	2.51	0.315	1.5 x 10 ⁻⁷ m s ⁻¹ for all the burn scars, and original values elsewhere.
Loamy sand	4.26	0.421	1.41E-5	3.83	0.392	
Sandy loam	4.74	0.434	5.23E-6	4.27	0.404	
Silt loam	5.33	0.476	2.81E-6	4.80	0.442	
Silt	3.86	0.484	2.18E-6	3.47	0.450	
Loam	5.25	0.439	3.38E-6	4.73	0.408	
Sandy clay loam	6.77	0.404	4.45E-6	6.09	0.376	
Silty clay loam	8.72	0.464	2.03E-6	7.85	0.432	
Clay loam	8.17	0.465	2.45E-6	7.35	0.432	
Sandy clay	10.73	0.406	7.22E-6	9.66	0.378	
Silty clay	10.39	0.468	1.34E-6	9.35	0.435	
Clay	11.55	0.468	9.74E-7	10.40	0.435	
Organic material	5.25	0.439	3.38E-6	4.73	0.408	
Water	0.00	1.00	0.00	0.00	1.00	
Bedrock	2.79	0.200	1.41E-4	2.51	0.186	
Other	4.26	0.421	1.41E-5	3.83	0.392	
Playa	11.55	0.468	9.74E-7	10.40	0.435	
Lava	2.79	0.200	1.41E-4	2.51	0.186	
White sand	2.79	0.339	4.66E-5	2.51	0.315	

970
 971 **Table B3** Soil parameters in default and calibrated WRF-Hydro. Default soil parameters in WRF-
 972 Hydro are adapted from the soil analysis by Cosby et al. (1984). Grain size distribution index and
 973 soil porosity are altered from default values during the global soil moisture calibration. Saturated
 974 hydraulic conductivity is altered from default values during the streamflow calibration.
 975

976



977
 978
 979 **Fig. B6** WRF-Hydro simulated discharge time-series at four debris flow source areas. (a)–(c)
 980 MRMS precipitation (green bars) and simulated discharge time-series for January 26th 00:00 to
 981 31st 23:00 at Mill Creek, Big Creek, and Nacimientos debris flow source areas (black circles in Fig.
 982 7b–d) in baseline (purple dashed line) and burn scar simulation (red line).

Formatted: Superscript

Formatted: Superscript

989 *Table B4*

990 *The total runoff volume, peak discharge, and peak timing at debris-flow source areas*

Site name	Baseline simulation			Burn scar simulation		
	Total volume (m ³)	Peak discharge (m ³ s ⁻¹)	Peak timing	Total volume (m ³)	Peak discharge (m ³ s ⁻¹)	Peak timing
Mill Creek	10,023	0.23	27 th 23:00	83,853 (+737%)	1.24 (+439%)	27 th 13:00
Big Creek	11,611	0.71	28 th 05:00	128,879 (+1010%)	2.81 (+296%)	28 th 05:00
Nacimiento	3,031	0.05	27 th 13:00	49,792 (+1542%)	0.76 (+1420%)	27 th 13:00

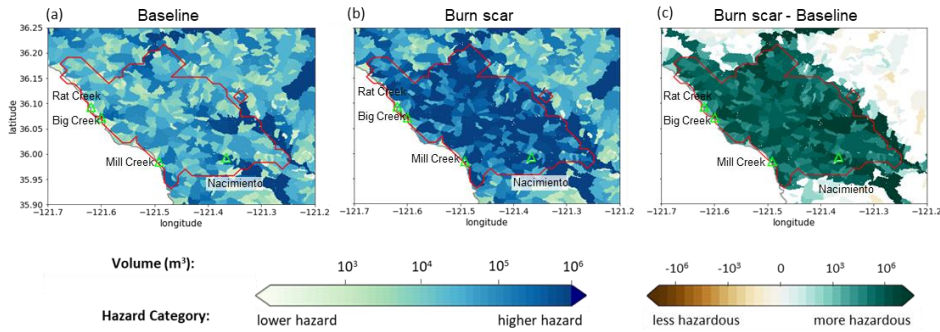
991 **Table B4** The total runoff volume, peak discharge, and peak timing in the baseline and burn scar
992 simulations from January 27th 00:00 to 31st 23:00 at source areas of Rat Creek, Mill Creek, Big
993 Creek, and Nacimiento debris flows (black circles in Fig. 7b–d). The percent change of the total
994 volume and peak discharge in the burn scar simulation relative to the baseline simulation are shown
995 in parentheses.

996

997

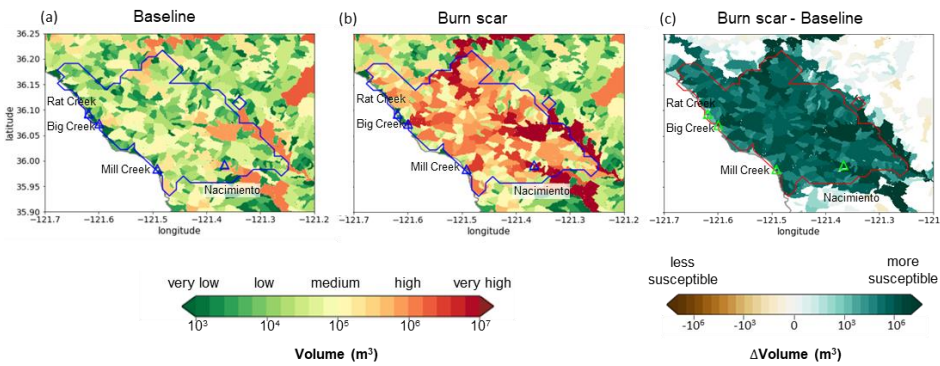
998

Non-normalized catchment hazard assessment



999

Non-normalized catchment postfire debris flow susceptibility



1000

1001

1002 **Fig. B7** Discharge volume-based runoff-generated debris flow hazard susceptibility at catchment
 1003 level in the (a) baseline simulation, (b) burn scar simulation, and (c) the difference between the
 1004 burn scar and baseline simulations. For each catchment, the hazard susceptibility is assessed by
 1005 computing the total discharge volume at the catchment outlet from January 27th 00:00 to 28th 12:00.

1006

1007

1008 Data availability statement

1009 The NLDAS-2 reanalysis forcing data is publicly available at NASA GES DISC:
 1010 <https://disc.gsfc.nasa.gov/datasets?keywords=NLDAS>. A detailed description can be found at

- Formatted: Superscript
- Formatted: Superscript
- Formatted: Font color: Auto

1011 <https://ldas.gsfc.nasa.gov/nldas/v2/forcing>. The MRMS radar-only precipitation estimate is
1012 publicly available at: <https://mtarchive.geol.iastate.edu/>. A description can be found at
1013 <https://www.nssl.noaa.gov/projects/mrms/>. The PSL in-situ soil moisture data is publicly available
1014 at: <https://psl.noaa.gov/data/obs/datadisply/>. The USGS streamflow is publicly available at:
1015 <https://waterdata.usgs.gov/nwis/>. The wildfire perimeter shapefiles are downloadable at:
1016 <https://data-nifc.opendata.arcgis.com/search?collection=Dataset>. The remote sensing data used in
1017 this manuscript were provided by the European Space Agency (ESA) Copernicus program and
1018 accessed on Google Earth Engine (<https://code.earthengine.google.com>). All processed data
1019 required to reproduce the results of this study are archived on Zenodo at
1020 <http://doi.org/10.5281/zenodo.5544083>.

1021 **Code availability statement**

1022 The modified WRF-Hydro Fortran code and instructions to output the overland flow at terrain
1023 routing grid can be downloaded at <https://github.com/NU-CCRG/Modified-WRF-Hydro>.

1024 HazMapper v1.0 is available at <https://hazmapper.org/>. The SAR backscatter change method code
1025 is available at https://github.com/MongHanHuang/GEE_SAR_landslide_detection.

1026 **Author contribution**

1027 Conceptualization: CL, ALH, & DEH; Simulation and model analysis: CL; JW & WY model
1028 methodological development. Remote sensing analysis: ALH; Field Observations: NJF; GIS
1029 assistance: YX; Funding acquisition: GB & DH; CL wrote the original draft and all authors
1030 reviewed and edited the manuscript.

1031 **Competing interests**

1032 The authors declare that they have no conflict of interest.

1033 **Acknowledgments**

1034 C.L., A.L.H., J.W., X.L., G.B., and D.E.H. acknowledge support from NSF PREEVENTS
1035 #1848683. We acknowledge high-performance computing support from Cheyenne
1036 (doi:10.5065/D6RX99HX) provided by NCAR's Computational and Information Systems
1037 Laboratory, sponsored by the National Science Foundation. We thank P. Santi, an anonymous
1038 reviewer, and the editor for formal reviews, and F. K. Rengers for informal comments.
1039

1041 **References**

- 1042 [Alfieri L., Salamon P., Pappenberger F., Wetterhall F., Thielen J. \(2012\). Operational early warning systems for](#)
 1043 [water-related hazards in Europe Environmental Science & Policy 21:35-49](#)
 1044 [doi:https://doi.org/10.1016/j.envsci.2012.01.008](#)
- 1045 Anderson, H. W., Hoover, M. D., & Reinhart, K. G. (1976). Forests and water: effects of forest management on
 1046 floods, sedimentation, and water supply (Vol. 18): Department of Agriculture, Forest Service, Pacific
 1047 Southwest Forest and Range Experiment Station, Berkeley, CA.
- 1048 Andersson, J. C. M., Arheimer, B., Traoré, F., Gustafsson, D., & Ali, A. (2017). Process refinements improve a
 1049 hydrological model concept applied to the Niger River basin. *Hydrological Processes*, 31(25), 4540-
 1050 4554. doi:https://doi.org/10.1002/hyp.11376
- 1051 Arattano, M., & Franzi, L. (2010). On the application of kinematic models to simulate the diffusive processes of
 1052 debris flows. *Nat. Hazards Earth Syst. Sci.*, 10(8), 1689-1695. doi:10.5194/nhess-10-1689-2010
- 1053 Arattano, M., & Savage, W. [Z. J. B. o. t. I. A. o. E. G. B. d. I. A. I. d. G. d. I. I. Z.](#) (1994). Modelling debris flows
 1054 as kinematic waves. [Bulletin of the International Association of Engineering Geology](#) 49, 3–13.
 1055 [https://doi.org/10.1007/BF02594995](#)
- 1056 [Banihabib, M. E., Jurik, L., Kazemi, M. S., Soltani, J., & Tanhapour, M. \(2020\). A Hybrid-Intelligence Model](#)
 1057 [for the Prediction of the Peak Flow of Debris Floods. Water, 12\(8\). doi:10.3390/w12082246](#)
- 1058 Bart, R. (2016). A regional estimate of postfire streamflow change in California. *Water Resources Research*, 52,
 1059 n/a-n/a. doi:10.1002/2014WR016553
- 1060 Bart, R., & Hope, A. (2010). Streamflow response to fire in large catchments of a Mediterranean-climate region
 1061 using paired-catchment experiments. *Journal of Hydrology*, 388, 370-378.
 1062 doi:10.1016/j.jhydrol.2010.05.016
- 1063 [Brabb E.E. \(1985\) Innovative approaches to landslide hazard and risk mapping. In: International Landslide](#)
 1064 [Symposium Proceedings, Toronto, Canada. pp 17-22](#)
- 1065 Bisson M., Favalli M., Fornaciai A., Mazzarini F., Isola I., Zanchetta G., & Pareschi M. (2005). A
 1066 rapid method to assess fire-related debris flow hazard in the Mediterranean region: An example from
 1067 Sicily (southern Italy) *International Journal of Applied Earth Observation and Geoinformation* 7:217-
 1068 231 doi:https://doi.org/10.1016/j.jag.2005.04.003
- 1069 Bitew, M. M., & Gebremichael, M. (2011). Assessment of satellite rainfall products for streamflow simulation
 1070 in medium watersheds of the Ethiopian highlands. *Hydrol. Earth Syst. Sci.*, 15(4), 1147-1155.
 1071 doi:10.5194/hess-15-1147-2011
- 1072 Brown, E.K., Wang, J., & Feng, Y. (2020). U.S. wildfire potential: a historical view and future projection using
 1073 high-resolution climate data. *Environmental Research Letters*. 16, 034060
- 1074 [Brunkal, H., & Santi, P. M. \(2016\). Exploration of design parameters for a dewatering structure for debris flow](#)
 1075 [mitigation. 208, 81-92.](#)
- 1076 Bytheway, J. L., Hughes, M., Mahoney, K., & Cifelli, R. (2020). On the Uncertainty of High-Resolution Hourly
 1077 Quantitative Precipitation Estimates in California, *Journal of Hydrometeorology*, 21(5), 865-879.
 1078 Retrieved Oct 25, 2021, from [https://journals.ametsoc.org/view/journals/hydr/21/5/jhm-d-19-](https://journals.ametsoc.org/view/journals/hydr/21/5/jhm-d-19-0160.1.xml)
 1079 [0160.1.xml](https://journals.ametsoc.org/view/journals/hydr/21/5/jhm-d-19-0160.1.xml)
- 1080 [Camera, Canfield, H. E., Goodrich, D. C., Bruggeman, A., Zittis, G., Sofokleous, I., & Arnault, J. \(2020\).](#)
 1081 [Simulation of extreme rainfall & Burns, I. S. \(2005\). Selection of parameters values to model post-fire](#)
 1082 [runoff and streamflow—event sediment transport at the watershed scale in small](#)
 1083 [Mediterranean southwestern forests. In Managing watersheds with a one-way-coupled-atmospheric-](#)

Formatted: Space Before: 0 pt

hydrologic modelling system. *Natural hazards for human and earth system sciences*, 20(10), 2791-2840. [natural impacts: engineering, ecological, and economic challenges \(pp. 1-12\).](#)

Canli E., Mergili M., Thiebes B., & Glade T. (2018) [Probabilistic landslide ensemble prediction systems: lessons to be learned from hydrology](#) *Nat Hazards Earth Syst Sci* 18:2183-2202 doi:10.5194/nhess-20-2791-2020/18-2183-2018

Canfield, H., Goodrich, D., & Burns, I. S. (2005). [Selection of Parameters Values to Model Postfire Runoff and Sediment Transport at the Watershed Scale in Southwestern Forests.](#)

Cannon, S.H., Kirkham R.M., & Paise M., (2001). [Wildfire-related debris-flow initiation processes.](#) *Storm King Mountain, Colorado. Geomorphology*, v.39, n. 3-4, 171-188

Cannon, S. H., Gartner, J., E., Parrett, C., P., & Parise, M. (2003). [Wildfire-related debris-flow generation through episodic progressive sediment-bulking processes, western USA \(Vol. 1\): Debris-Flow Hazards Mitigation: Mechanics, Prediction, and Assessment.](#) Millpress, Rotterdam, pp. 71-82.

Cannon, S. H., Gartner, J., Wilson, R., Bowers, J., & Laber, J. (2008). Storm Rainfall Conditions for Floods and Debris Flows from Recently Burned Basins in Southwestern Colorado and Southern California. *Geomorphology*, 96, 250-269. doi:10.1016/j.geomorph.2007.03.019

Cannon, S. H. (2001). [Debris flow generation from recently burned watersheds.](#) *Environmental & Engineering Geoscience*, 7(4), 321-341.

Cannon, S. H., Boldt, E. M., Laber, J. L., Kean, J. W., & Staley, D. M. J. N. H. (2011). [Rainfall intensity-duration thresholds for postfire debris flow emergency-response planning.](#) 59(1), 209-236.

Cannon, S. H., & DeGraff, J. (2009). The increasing wildfire and postfire debris flow threat in western USA, and implications for consequences of climate change. In *Landslides-disaster risk reduction* (pp. 177-190): Springer.

Cannon, S. H., Gartner, J. E., Rupert, M. G., Michael, J. A., Rea, A. H., & Parrett, C. (2010). Predicting the probability and volume of postwildfire debris flows in the intermountain western United States. *GSA Bulletin*, 122(1-2), 127-144. doi:10.1130/B26459.1

Cannon, S. H., Boldt, E. M., Laber, J. L., Kean, J. W., & Staley, D. M. J. N. H. (2011). [Rainfall intensity-duration thresholds for postfire debris flow emergency-response planning.](#) 59(1), 209-236.

Cavagnaro, D. et al. (2021) [Variability in hydrologic response to rainfall across a burn scar: observations from the Dolan Fire, California.](#) AGU abstract. <https://agu.confex.com/agu/fm21/meetingapp.cgi/Paper/921613>

Cerdà, A. (1998). Changes in overland flow and infiltration after a rangeland fire in a Mediterranean scrubland. *Hydrological Processes*, 12(7), 1031-1042. doi:https://doi.org/10.1002/(SICI)1099-1085(19980615)12:7<1031::AID-HYP636>3.0.CO;2-V

Chen, F., & Dudhia, J. (2001). Coupling an Advanced Land Surface-Hydrology Model with the Penn State-NCAR MM5 Modeling System. Part I: Model Implementation and Sensitivity, *Monthly Weather Review*, 129(4), 569-585. Retrieved Oct 24, 2021, from https://journals.ametsoc.org/view/journals/mwre/129/4/1520-0493_2001_129_0569_caalsh_2.0.co_2.xml

Chen, L., Berli, M., & Chief, K. (2013). Examining Modeling Approaches for the Rainfall-Runoff Process in Wildfire-Affected Watersheds: Using San Dimas Experimental Forest. *JAWRA Journal of the American Water Resources Association*, 49(4), 851-866. doi:https://doi.org/10.1111/jawr.12043

Claessens L., Schoorl, J.M., & Veldkamp, A. (2007) [Modelling the location of shallow landslides and their effects on landscape dynamics in large watersheds: An application for Northern New Zealand](#) *Geomorphology* 87:16-27 doi:https://doi.org/10.1016/j.geomorph.2006.06.039

Crosta G. B., & Frattini P. (2003) [Distributed modelling of shallow landslides triggered by intense rainfall.](#) *Nat Hazards Earth Syst Sci* 3:81-93 doi:10.5194/nhess-3-81-2003

130 [Cui, Y., Cheng, D., & Chan, D. \(2018\). Investigation of post-fire debris flows in Montecito. *ISPRS International*](#)
131 [Journal of Geo-Information, 8\(1\), 5.](#)

132 ~~Reynolds, C., (2021, February 25). Highway 1 washout near Big Sur expected to be fixed by summer, Los~~
133 ~~Angeles Times. <https://www.latimes.com/travel/story/2021-02-25/highway-1-to-big-sur-will-reopen>~~
134 ~~by summer caltrans says~~

1135 Coe, J., Godt, J., Parise, M., & Moscariello, A. (2003). Estimating debris flow probability using fan stratigraphy,
1136 historic records, and drainage-basin morphology, Interstate 70 highway corridor, central Colorado, USA.
1137 Paper presented at the Debris flow Hazards Mitigation: Mechanics, Prediction, and Assessment, edited
1138 by: Rickenmann, D. and Cheng, Ch., Proceedings 3rd International DFHM Conference, Davos,
1139 Switzerland.

1140 Coe, J. A., Kinner, D. A., & Godt, J. W. J. G. (2008). Initiation conditions for debris flows generated by runoff
1141 at Chalk Cliffs, central Colorado. 96(3-4), 270-297.

1142 Cosby, B. J., Hornberger, G. M., Clapp, R. B., & Ginn, T. R. (1984). A Statistical Exploration of the
1143 Relationships of Soil Moisture Characteristics to the Physical Properties of Soils. *Water Resources*
1144 *Research*, 20(6), 682-690. doi:https://doi.org/10.1029/WR020i006p00682

1145 Cydzik, K., & Hogue, T. ~~SS-I J. J. o. t. A. W. R. A.~~ (2009). Modeling postfire response and recovery using the
1146 hydrologic engineering center hydrologic modeling system (HEC - HMS) 1. *JAWRA Journal of the*
1147 *American Water Resources Association*, 45(3), 702-714.

1148 [Dahal, R.K., Hasegawa, S., Nonomura, A., Yamanaka, M., Dhakal, S., Paudyal, P. \(2008\) Predictive modelling](#)
1149 [of rainfall-induced landslide hazard in the Lesser Himalaya of Nepal based on weights-of-evidence](#)
1150 [Geomorphology 102:496-510 doi:https://doi.org/10.1016/j.geomorph.2008.05.041](#)

1151 Daly, C., R. P. Neilson, & D. L. Phillips. (1994). A statistical-topographic model for mapping climatological
1152 precipitation over mountainous terrain. *J. Appl. Meteor.*, 33, 140–158, [https://doi.org/10.1175/1520-](https://doi.org/10.1175/1520-0450(1994)033<0140:ASTMFM>2.0.CO;2)
1153 [0450\(1994\)033<0140:ASTMFM>2.0.CO;2](https://doi.org/10.1175/1520-0450(1994)033<0140:ASTMFM>2.0.CO;2)

1154 Daly, C., M. E. Slater, J. A. Roberti, S. H. Laseter, & L. W. Swift Jr. (2017). High-resolution precipitation
1155 mapping in a mountainous watershed; Ground truth for evaluating uncertainty in a national precipitation
1156 dataset. *Int. J. Climatol.*, 37, 124–137, <https://doi.org/10.1002/joc.4986>.

1157 Davies, T., Phillips, C., Pearce, A., & Zhang, X. J. I. P. (1992). Debris flow behaviour—an integrated overview.
1158 209(21), 225.

1159 Dekker, L. W., & Ritsema, C. J. (1994). How water moves in a water repellent sandy soil: 1. Potential and actual
1160 water repellency. *Water Resources Research*, 30(9), 2507-2517.
1161 doi:https://doi.org/10.1029/94WR00749

1162 [Deser, C. et al. \(2020\) Insights from Earth system model initial-condition large ensembles and future prospects](#)
1163 [Nature Climate Change 10:277-286 doi:10.1038/s41558-020-0731-2](#)

1164 Di Cristo, C., Iervolino, M., Moramarco, T., & Vacca, A. (2021). Applicability of Diffusive model for mud-
1165 flows: An unsteady analysis. *Journal of Hydrology*, 600, 126512.
1166 doi:https://doi.org/10.1016/j.jhydrol.2021.126512

1167 Doerr, S. H., & Thomas, A. (2000). The role of soil moisture in controlling water repellency: New evidence
1168 from forest soils in Portugal. *Journal of Hydrology*, 231-232, 134-147. doi:10.1016/S0022-
1169 1694(00)00190-6

1170 [Flannigan, M., Cantin, A. S., De Groot, W. J., Wotton, M., Newbery, A., & Gowman, L. M. \(2013\). Global](#)
1171 [wildland fire season severity in the 21st century. *Forest Ecology and Management*, 294, 54-61.](#)

1172 Friedel, M.J. (2011a). A data-driven approach for modeling post-fire debris-flow volumes and their uncertainty
1173 *Environmental Modelling & Software* 26:1583-1598 doi:https://doi.org/10.1016/j.envsoft.2011.07.014

Formatted: Superscript

Formatted: Font: Cambria Math

Formatted: Font: 10 pt

1174 Friedel, M.J. (2011b) Modeling hydrologic and geomorphic hazards across post-fire landscapes using a self-
1175 organizing map approach Environmental Modelling & Software 26:1660-1674
1176 doi:<https://doi.org/10.1016/j.envsoft.2011.07.001>

1177 Gartner, J. E., Cannon, S. H., & Santi, P. M. (2014). Empirical models for predicting volumes of sediment
1178 deposited by debris flows and sediment-laden floods in the transverse ranges of southern California.
1179 Engineering Geology, 176, 45-56. doi:<https://doi.org/10.1016/j.enggeo.2014.04.008>

1180 George, D. L., & Iverson, R. M. (2014). A depth-averaged debris flow model that includes the effects of evolving
1181 dilatancy. II. Numerical predictions and experimental tests. Proceedings of the Royal Society A:
1182 Mathematical, Physical and Engineering Sciences, 470(2170), 20130820. doi:10.1098/rspa.2013.0820

1183 Gochis, D. J., & Chen, F. (2003). Hydrological Enhancements to the Community Noah Land Surface Model (No.
1184 NCAR/TN-454+STR). University Corporation for Atmospheric Research. doi:10.5065/D60P0X00

1185 Goodrich, D., Burns, I., Unkrich, C., Semmens, D., Guertin, D., Hernandez, M., . . . Levick, L. (2012).
1186 KINEROS2/AGWA: model use, calibration, and validation. Transactions of the ASABE, 55, 1561-
1187 1574. doi:10.13031/2013.42264

1188 Goss, M., Swain, D. L., Abatzoglou, J. T., Sarhadi, A., Kolden, C. A., Williams, A. P., & Diffenbaugh, N. S.
1189 (2020). Climate change is increasing the likelihood of extreme autumn wildfire conditions across
1190 California. Environmental Research Letters, 15(9), 094016. doi:10.1088/1748-9326/ab83a7

1191 Gregoretti, C., & Fontana, G. D. Dalla Fontana, G. (2007). [Rainfall threshold for the initiation of debris flows by](#)
1192 [channel-bed failure in the Dolomites. Debris-Flow Hazards Mitigation: Mechanics, Prediction, and](#)
1193 [Assessment, 11-22.](#)

1194 [Gregoretti, C., & Dalla Fontana, G. \(2008\). The triggering of debris flow due to channel-bed failure in some](#)
1195 [alpine headwater basins of the Dolomites: analyses of critical runoff. Hydrological Processes, 22\(13\),](#)
1196 [2248-2263. doi:https://doi.org/10.1002/hyp.6821](#)

1197 Gupta, H. V., Kling, H., Yilmaz, K. K., & Martinez, G. F. (2009). Decomposition of the mean squared error and
1198 NSE performance criteria: Implications for improving hydrological modelling. Journal of Hydrology,
1199 377(1), 80-91. doi:<https://doi.org/10.1016/j.jhydrol.2009.08.003>

1200 [Guzzetti, F., Reichenbach, P., Cardinali, M., Galli, M., & Ardizzone, F. J. G. \(2005\) Probabilistic landslide](#)
1201 [hazard assessment at the basin scale 72:272-299](#)

1202 Handwerker, A. L., [Huang, M.-H.](#), Jones, S. Y., Amatya, P., Kerner, H. R., ~~and~~ Kirschbaum, D. B., ~~and~~. (2022)
1203 [Generating landslide density heatmaps](#) [Huang, M. H. \(in review\): Strategies for landslide rapid](#)
1204 [detection using open-access synthetic aperture satellite radar backscatter change data in Google Earth Engine, Nat.](#)
1205 [Hazards Earth Syst. Sci. Discuss. doi:10.5194/nhess-2021-283](#)

1206 [Hapuarachchi, H.A.P., Wang, Q.J., & Pagano, T.C. \(2011\) A review of advances in flash flood forecasting.](#)
1207 [Hydrological processes. 25:2771-2784 doi:https://doi.org/10.1002/hyp.8040](#)

1208 [Hawkins, E., Sutton, R. \(2009\) The Potential to Narrow Uncertainty in Regional Climate Predictions Bull Amer](#)
1209 [Meteor Soc 90:1095-1108 doi:10.1175/2009BAMS2607.1](#)

1210 Huang, X., Swain, D. L., & Hall, A. D. (2020). Future precipitation increase from very high resolution ensemble
1211 downscaling of extreme atmospheric river storms in California. 6(29), eaba1323.
1212 doi:10.1126/sciadv.aba1323 %J Science Advances

1213 Ice, G. G., Neary, D. G., & Adams, P. W. (2004). Effects of Wildfire on Soils and Watershed Processes. Journal
1214 of Forestry, 102(6), 16-20. doi:10.1093/jof/102.6.16

1215 Iverson, R. M., & George, D. L. (2014). A depth-averaged debris flow model that includes the effects of evolving
1216 dilatancy. I. Physical basis. Proceedings of the Royal Society A: Mathematical, Physical and
1217 Engineering Sciences, 470(2170), 20130819. doi:10.1098/rspa.2013.0819

1218 Jolly, W. M., Cochrane, M. A., Freeborn, P. H., Holden, Z. A., Brown, T. J., Williamson, G. J., & Bowman, D.
1219 M. J. S. (2015). Climate-induced variations in global wildfire danger from 1979 to 2013. *Nature*
1220 *Communications*, 6(1), 7537. doi:10.1038/ncomms8537

1221 Julien, P. Y., Saghafian, B., & Ogden, F. L. (1995). RASTER-BASED HYDROLOGIC MODELING OF
1222 SPATIALLY-VARIED SURFACE RUNOFF1. *JAWRA Journal of the American Water Resources*
1223 *Association*, 31(3), 523-536. doi:https://doi.org/10.1111/j.1752-1688.1995.tb04039.x

1224 Kean, J. W., Staley, D. M., & Cannon, S. H. (2011). In situ measurements of postfire debris flows in southern
1225 California: Comparisons of the timing and magnitude of 24 debris flow events with rainfall and soil
1226 moisture conditions. *Journal of Geophysical Research F: Earth Surface*, 116(4).
1227 doi:10.1029/2011JF002005

1228 Kean, J. W., McCoy, S. W., Tucker, G. E., Staley, D. M., & Coe, J. A. (2013). Runoff-generated debris flows:
1229 Observations and modeling of surge initiation, magnitude, and frequency. *Journal of Geophysical*
1230 *Research: Earth Surface*, 118(4), 2190-2207. doi:https://doi.org/10.1002/jgrf.20148

1231 Kean, J. W., & Staley, D. M. (2021). Forecasting the Frequency and Magnitude of Postfire Debris Flows Across
1232 Southern California. *Earth's Future*, 9(3), e2020EF001735. doi:https://doi.org/10.1029/2020EF001735

1233 ~~Kean, J. W., Staley, D. M., & Cannon, S. H. (2011). In situ measurements of postfire debris flows in southern~~
1234 ~~California: Comparisons of the timing and magnitude of 24 debris flow events with rainfall and soil~~
1235 ~~moisture conditions. *Journal of Geophysical Research F: Earth Surface*, 116(4).~~
1236 ~~doi:10.1029/2011JF002005~~

1237 Kinoshita, A. M., & Hogue, T. S. (2015). Increased dry season water yield in burned watersheds in Southern
1238 California. *Environmental Research Letters*, 10(1), 014003. doi:10.1088/1748-9326/10/1/014003

1239 Kling, H., Fuchs, M., & Paulin, M. (2012). Runoff conditions in the upper Danube basin under an ensemble of
1240 climate change scenarios. *Journal of Hydrology*, 424-425, 264-277.
1241 doi:https://doi.org/10.1016/j.jhydrol.2012.01.011

1242 Larsen, I., MacDonald, L., Brown, E., Rough, D., Welsh, M., Pietraszek, J., . . . Schaffrath, K. (2009). Causes
1243 of Postfire Runoff and Erosion: Water Repellency, Cover, or Soil Sealing? *Soil Science Society of*
1244 *America Journal - SSSAJ*, 73. doi:10.2136/sssaj2007.0432

1245 Lahmers, T. M., Gupta, H., Castro, C. L., Gochis, D. J., Yates, D., Dugger, A., . . . Hazenberg, P. J. J. o. H.
1246 (2019). Enhancing the structure of the WRF-Hydro hydrologic model for semiarid environments. 20(4),
1247 691-714.

1248 Lahmers, T. M., Castro, C. L., & Hazenberg, P. (2020). Effects of Lateral Flow on the Convective Environment
1249 in a Coupled Hydrometeorological Modeling System in a Semiarid Environment, *Journal of*
1250 *Hydrometeorology*, 21(4), 615-642. Retrieved Sep 29, 2021, from
1251 [https://journals.ametsoc.org/view/journals/hydr/21/4/jhm-d-19-](https://journals.ametsoc.org/view/journals/hydr/21/4/jhm-d-19-0100-1.xml)
1252 [0100-1.xml](https://journals.ametsoc.org/view/journals/hydr/21/4/jhm-d-19-0100-1.xml)<https://journals.ametsoc.org/view/journals/hydr/21/4/jhm-d-19-0100-1.xml>

1253 MacDonald, L. H., & Huffman, E. L. (2004). Postfire soil water repellency: Persistence and soil moisture
1254 thresholds. *Soil Science Society of America Journal*, 68, 1729-1734.

1255 Martin, D., & Moody, J. (2001). Comparison of Soil Infiltration Rates in Burned and Unburned Mountainous
1256 Watersheds. *Hydrological Processes*, 15, 2893-2903. doi:10.1002/hyp.380

1257 McGuire, L. A., J. W. Kean, D. M. Staley, F. K. Rengers, and T. A. Wasklewicz (2016), Constraining the relative
1258 importance of raindrop- and flow-driven sediment transport mechanisms in postwildfire environments
1259 and implications for recovery time scales, *J. Geophys. Res. Earth Surf.*, 121, 2211– 2237,
1260 doi:10.1002/2016JF003867

1261 McGuire, L. A., Rengers, F. K., Kean, J. W., & Staley, D. M. (2017). Debris flow initiation by runoff in a
1262 recently burned basin: Is grain-by-grain sediment bulking or en masse failure to blame? *Geophysical*
1263 *Research Letters*, 44(14), 7310-7319. doi:https://doi.org/10.1002/2017GL074243

1264 McGuiire, L. A., & Youberg, A. M. (2020). What drives spatial variability in rainfall intensity-duration thresholds
1265 for post-wildfire debris flows? Insights from the 2018 Buzzard Fire, NM, USA. *Landslides*, 17(10),
1266 2385-2399. doi:10.1007/s10346-020-01470-y

1267 McMichael, C. E., & Hope, A. S. (2007). Predicting streamflow response to fire-induced landcover change:
1268 implications of parameter uncertainty in the MIKE SHE model. *J Environ Manage*, 84(3), 245-256.
1269 doi:10.1016/j.jenvman.2006.06.003

1270 Meixner, T., & Wohlgemuth, P. (2003). ~~Climate Variability, Fire, Vegetation Recovery, and Watershed~~
1271 ~~Hydrology~~. M. (2003). ~~Climate variability, fire, vegetation recovery, and watershed hydrology. In~~
1272 ~~Proceedings of the First Interagency Conference on Research in the Watersheds, Benson, Arizona (pp.~~
1273 ~~651-656).~~

1274 Meyer, G. A., & Wells, S. G. (1997). Fire-related sedimentation events on alluvial fans, Yellowstone National
1275 Park, U.S.A. *Journal of Sedimentary Research*, 67(5), 776-791. doi:10.1306/D426863A-2B26-11D7-
1276 8648000102C1865D

1277 Mikoš, M., & Bezak, N. (2021). ~~Debris Flow Modelling Using RAMMS Model in the Alpine Environment With~~
1278 ~~Focus on the Model Parameters and Main Characteristics~~. 8(732). doi:10.3389/feart.2020.605064

1279 Miller, D. A., & White, R. A. (1998). A Conterminous United States Multilayer Soil Characteristics Dataset for
1280 Regional Climate and Hydrology Modeling, *Earth Interactions*, 2(2), 1-26. Retrieved Sep 27, 2021, from
1281 https://journals.ametsoc.org/view/journals/eint/2/2/1087-3562_1998_002_0001_acusms_2.3.co_2.xml

1282 Mitsopoulos, I. D., & Mironidis, D. (2006). Assessment of post fire debris flow potential in a Mediterranean
1283 type ecosystem. *WIT Transactions on Ecology and the Environment*, 90.

1284 Moody, J. A., Shakesby, R. A., Robichaud, P. R., Cannon, S. H., & Martin, D. A. (2013). ~~Current research issues~~
1285 ~~related to post-wildfire runoff and erosion processes~~. , & Ebel, B. *Earth Science Reviews*, 122, 10-37.
1286 doi:<https://doi.org/10.1016/j.earscirev.2013.03.004> (2012). ~~Hyper-dry conditions provide new insights~~
1287 ~~into the cause of extreme floods after wildfire~~. *CATENA*, 93, 58-63. doi:10.1016/j.catena.2012.01.006

1288 Moody, J., Shakesby, R., Robichaud, P., Cannon, S., & Martin, D. A. J. E. S. R. (2013). ~~Current research issues~~
1289 ~~related to post-wildfire runoff and erosion processes~~. 122, 10-37.

1290 Moriasi, D. N., Arnold, J. G., Van Liew, M. W., Bingner, R. L., Harmel, R. D., & Veith, T. L. (2007). Model
1291 evaluation guidelines for systematic quantification of accuracy in watershed simulations. *Transactions*
1292 *of the ASABE*, 50(3), 885-900.

1293 Nash, J. E., & Sutcliffe, J. V. (1970). River flow forecasting through conceptual models part I — A discussion
1294 of principles. *Journal of Hydrology*, 10(3), 282-290. doi:[https://doi.org/10.1016/0022-1694\(70\)90255-](https://doi.org/10.1016/0022-1694(70)90255-6)
1295 6

1296 Neary, D. G., Gottfried, G. J., & Ffolliott, P. F. (2003). Post-wildfire watershed flood responses. *In Proceedings*
1297 *of the 2nd International Fire Ecology Conference, Orlando, Florida (pp. 16-20)*.

1298 Nikolopoulos, E.I., Destro, E., Bhuiyan, M.A.E, Borga, M., & Anagnostou, E.N. (2018). Evaluation of predictive
1299 models for postfire debris flow occurrence in the western United States *Nat Hazards Earth Syst Sci*
1300 18:2331-2343 doi:10.5194/nhess-18-2331-2018

1301 Nikolopoulos, E.I., Schwartz, C., Zhang, X., & Anagnostou, E.N. (2019) *Rainfall estimation uncertainty and*
1302 *early warning procedures for post-fire debris flows. In: Geophysical Research Abstracts.*

1303 Niu, G.-Y et al. (2011) The community Noah land surface model with multiparameterization options (Noah-MP):
1304 1. Model description and evaluation with local-scale measurements *J Geophys Res Atm* 116
1305 doi:<https://doi.org/10.1029/2010JD015139>

1306 Nyman, P., Smith, H.-G., Sherwin, C.-B., Langhans, C., Lane, P.-N. J., & Sheridan, G.-J. (2015). Predicting
1307 sediment delivery from debris flows after wildfire. *Geomorphology*, 250, 173-186.
1308 doi:<https://doi.org/10.1016/j.geomorph.2015.08.023>

1309 Oakley, N.S. (2021). A warming climate adds complexity to postfire hydrologic hazard planning. *Earth's Future*,
1310 9, e2021EF002149. <https://doi.org/10.1029/2021EF002149>

1311 Ogden, F.L. (1997). ~~CASC2D reference manual~~. L. J. D. o. C., Department of Civil & Environmental
1312 Engineering, U-o-C., University of Connecticut, Storrs. ~~(1997). CASC2D reference manual~~.

1313 Palmer, J. (2022). The devastating mudslides that follow forest fires. *Nature*.
1314 <https://www.nature.com/articles/d41586-022-00028-3>.

1315 Parise, M., & Cannon, S.H. (2008) The effects of wildfires on erosion and debris-flow generation in
1316 Mediterranean climatic areas: a first database. Proceedings of 1st World Landslide Forum. Tokyo, Japan,
1317 pp 465–468

1318 Parise, M., & Cannon, S.–H. (2009, ~~April~~). A database on post-fire erosion rates and debris flows in
1319 Mediterranean-Basin watersheds. In EGU General Assembly ~~Conference~~, Abstracts (p. 1530).

1320 Parise, M., & Cannon, S.H. (2012) Wildfire impacts on the processes that generate debris flows in burned
1321 watersheds *Nat Hazards* 61:217-227 doi:10.1007/s11069-011-9769-9

1322 Park, D.W., Lee, S.R., Vasu, N.N., Kang, S.H., Park, J.Y. (2016) Coupled model for simulation of landslides
1323 and debris flows at local scale *Nat Hazards* 81:1653-1682 doi:10.1007/s11069-016-2150-2

1324 Polade, S.D., Gershunov, A., Cayan, D.R., Dettinger, M.D., & Pierce, D.W. (2017) Precipitation in a
1325 warming world: Assessing projected hydro-climate changes in California and other Mediterranean
1326 climate regions *Scientific Reports* 7:10783 doi:10.1038/s41598-017-11285-y

1327 Qi, Y., S-Martinaitis, J.S., Zhang, & S.J., & Cocks, S. (2016). A real-time automated quality control of hourly
1328 rain gauge data based on multiple sensors in MRMS system. *J. Hydrometeor.*, 17, 1675–1691,
1329 <https://doi.org/10.1175/JHM-D-15-0188.1>.

1330 Raia, S., Alvioli, M., Rossi, M., Baum, R. L., Godt, J.W., Guzzetti, F. (2014) Improving predictive power of
1331 physically based rainfall-induced shallow landslide models: a probabilistic approach *Geosci Model Dev*
1332 7:495-514 doi:10.5194/gmd-7-495-2014

1333 Regmi, N.R., Giardino, J.R., Vitek, J.D. (2010) Modeling susceptibility to landslides using the weight of
1334 evidence approach: Western Colorado, USA *Geomorphology* 115:172-187
1335 doi:<https://doi.org/10.1016/j.geomorph.2009.10.002>

1336 Reichenbach, P., Rossi, M., Malamud, B.D., Mihir, M., Guzzetti, F. (2018) A review of statistically-based
1337 landslide susceptibility models *Earth-Science Reviews* 180:60-91
1338 doi:<https://doi.org/10.1016/j.earscirev.2018.03.001>

1339 Rengers, F.-K., McGuire, L.-A., Kean, J.-W., Staley, D.-M., & Hobbey, D.-E.-J. (2016). Model simulations of
1340 flood and debris flow timing in steep catchments after wildfire. *Water Resources Research*, 52(8), 6041-
1341 6061. doi:<https://doi.org/10.1002/2015WR018176>

1342 Reneau, S.L., Katzman, D., Kuyumjian, G.A., Lavine, A., & Malmon, D.V. (2007). Sediment delivery after a
1343 wildfire. *Geology*, 35(2), 151-154. doi:10.1130/G23288A.1

1344 Reynolds, C. (2021). Highway 1 washout near Big Sur expected to be fixed by summer. *Los Angeles Times*.
1345 <https://www.latimes.com/travel/story/2021-02-25/highway-1-to-big-sur-will-reopen-by-summer-caltrans-says>

1346

1347 Robichaud, P., Beyers, J., & Neary, D. (2000). Evaluating the effectiveness of postfire rehabilitation treatments.

1348 Rosso, R., Rulli, M.C., Bocchiola, D. (2007) Transient catchment hydrology after wildfires in a
1349 Mediterranean basin: runoff, sediment and woody debris *Hydrol Earth Syst Sci* 11:125-140
1350 doi:10.5194/hess-11-125-2007

1351 Rulli, M.-C., & Rosso, R. (2007). Hydrologic response of upland catchments to wildfires. *Advances in Water*
1352 *Resources*, 30(10), 2072-2086. doi:<https://doi.org/10.1016/j.advwatres.2006.10.012>

1353 Santi, P.-M., deWolfe, V.-G., Higgins, J.-D., Cannon, S.-H., & Gartner, J.-E. (2008). Sources of debris flow
1354 material in burned areas. *Geomorphology*, 96(3-4), 310-321. doi:10.1016/j.geomorph.2007.02.022

Formatted: Font: 10 pt

1355 Santi, P.-M., & Morandi, L. (2013). Comparison of debris flow volumes from burned and unburned areas.
1356 Landslides, 10(6), 757-769.

1357 Schaeffli, B., & Gupta, H. V. (2007). Do Nash values have value? Hydrological Processes, 21(15), 2075-2080.
1358 <https://doi.org/10.1002/hyp.6825>

1359 Scheip, C.-M., & Wegmann, K.-W. (2021). HazMapper: A global open-source natural hazard mapping
1360 application in Google Earth Engine. Natural Hazards and Earth System Sciences, 21(5), 1495-1511.

1361 Schönfelder, L. H., Bakken, T. H., Alfredsen, K., & Adera, A. G. (2017). Application of HYPE in Norway.
1362 [SINTEF Energi. Rapport.](#)

1363 Scott, D. F., & Van Wyk, D. B. (1990). The effects of wildfire on soil wettability and hydrological behaviour of
1364 an afforested catchment. 121, 239. doi:10.1016/0022-1694(90)90234-o

1365 Scott, D. J. J. o. HE. (1993). The hydrological effects of fire in South African mountain catchments. [150:Journal](#)
1366 [of hydrology, 150\(2-4\)](#), 409-432.

1367 Shakesby, R. A., & Doerr, S. H. (2006). Wildfire as a hydrological and geomorphological agent. Earth-Science
1368 Reviews, 74(3), 269-307. doi:<https://doi.org/10.1016/j.earscirev.2005.10.006>

1369 Shen H., Lynch, B., Poulsen, C.J., & Yanites, B.J. (2021) A modeling framework (WRF-Landlab) for
1370 simulating orogen-scale climate-erosion coupling Computers & Geosciences 146:104625
1371 doi:<https://doi.org/10.1016/j.cageo.2020.104625>

1372 Sidman, G., Guertin, D., Goodrich, D., Unkrich, C., & Burns, I. (2016). Risk assessment of post-wildfire
1373 hydrological response in semiarid basins: the effects of varying rainfall representations in the
1374 KINEROS2/AGWA model. International Journal of Wildland Fire, 25, 268-278. doi:10.1071/WF14071

1375 Staley, D. M., Negri, J. A., Kean, J. W., Laber, J. L., Tillery, A. C., & Youberg, A. M. (2016). Updated logistic
1376 regression equations for the calculation of postfire debris flow likelihood in the western United States
1377 (2016-1106). Retrieved from Reston, VA: <http://pubs.er.usgs.gov/publication/ofr20161106>

1378 [Staley, D.M., Negri, J.A., Kean, J.W., Laber, J.L., Tillery, A.C., & Youberg, A. M. \(2017\) Prediction of spatially](#)
1379 [explicit rainfall intensity-duration thresholds for post-fire debris-flow generation in the western United](#)
1380 [States Geomorphology 278:149-162 doi:https://doi.org/10.1016/j.geomorph.2016.10.019](#)

1381 Stoof, C.-R., Vervoort, R.-W., Iwema, J., van den Elsen, E., Ferreira, A.-J.-D., & Ritsema, C.-J. (2012).
1382 Hydrological response of a small catchment burned by experimental fire. Hydrol. Earth Syst. Sci., 16(2),
1383 267-285. doi:10.5194/hess-16-267-2012

1384 ~~Swain, D.L., Langenbrunner, B., Neelin, J.D., & Hall, A. (2018) Increasing precipitation volatility in twenty-~~
1385 ~~first-century California. Nature Climate Change. 8:427-433 doi:10.1038/s41558-018-0140-y~~

1386 ~~Swain, D.L.~~ (2021). A Shorter, Sharper Rainy Season Amplifies California Wildfire Risk. Geophysical
1387 Research Letters, 48(5), e2021GL092843. doi:<https://doi.org/10.1029/2021GL092843>

1388 ~~Swain, D. L., Tang, H., McGuire, L. A., Rengers, F. K., Kean, J. W., Staley, D. M., & Smith, J. B. (2019).~~
1389 ~~Developing and testing physically based triggering thresholds for runoff-generated debris flows.~~
1390 ~~Geophysical Research Letters, 46, 8830– 8839. https://doi.org/10.1029/2019GL083623~~

1391 ~~Langenbrunner, B., Neelin, J. D., & Hall, A. (2018) Increasing precipitation volatility in twenty-first-century~~
1392 ~~California Nature Climate Change 8:427-433 doi:10.1038/s41558-018-0140-y~~

1393 Tognacca, C., Bezzola, G.R., & Minor, H.-E. (2000). Threshold criterion for debris-flow initiation due to
1394 channel-bed failure. ~~Paper presented at the~~ Debris-flow hazards mitigation: Mechanics, prediction and
1395 assessment. (pp. 89-97).

1396 U.S. Forest Service, Burned Area Emergency Response, Dolan Postfire BAER Soil Burn Severity Map Released,
1397 October 10, 2020, [https://inciweb.nwcg.gov/photos/CALPF/2020-10-06-1821-Dolan-PostFire-](https://inciweb.nwcg.gov/photos/CALPF/2020-10-06-1821-Dolan-PostFire-BAER/related_files/pict20200910-143346-0.pdf)
1398 [BAER/related_files/pict20200910-143346-0.pdf](https://inciweb.nwcg.gov/photos/CALPF/2020-10-06-1821-Dolan-PostFire-BAER/related_files/pict20200910-143346-0.pdf)

1399 U.S. Forest Service, Burned Area Emergency Response, Dolan Fire Burned Area Report, October 13, 2020,
1400 [https://inciweb.nwcg.gov/photos/CALPF/2020-10-06-1821-Dolan-PostFire-](https://inciweb.nwcg.gov/photos/CALPF/2020-10-06-1821-Dolan-PostFire-BAER/related_files/pict20200927-132609-0.pdf)
1401 [BAER/related_files/pict20200927-132609-0.pdf](https://inciweb.nwcg.gov/photos/CALPF/2020-10-06-1821-Dolan-PostFire-BAER/related_files/pict20200927-132609-0.pdf)

1402 U.S. Geological Survey, Postfire Debris flow Hazards: Dolan Fire (Los Padres National Forest, CA), Landslide
1403 Hazards Program, retrieved September 27, 2021, from
1404 https://landslides.usgs.gov/hazards/postfire_debrisflow/detail.php?objectid=312

1405 Vergopolan, N., Chaney, N.-W., Beck, H.-E., Pan, M., Sheffield, J., Chan, S., & Wood, E.-F. (2020). Combining
1406 hyper-resolution land surface modeling with SMAP brightness temperatures to obtain 30-m soil
1407 moisture estimates. *Remote Sensing of Environment*, 242, 111740.
1408 doi:<https://doi.org/10.1016/j.rse.2020.111740>

1409 Wang, J., Wang, C., Rao, V., Orr, A., Yan, E., & Kotamarthi, R. (2019). A parallel workflow implementation
1410 for PEST version 13.6 in high-performance computing for WRF-Hydro version 5.0: a case study over
1411 the midwestern United States. *Geoscientific Model Development*, 12(8), 3523-3539. doi:10.5194/gmd-
1412 12-3523-2019

1413 Williams, A.-P., Abatzoglou, J.-T., Gershunov, A., Guzman-Morales, J., Bishop, D.-A., Balch, J.-K., &
1414 Lettenmaier, D.-P. (2019). Observed Impacts of Anthropogenic Climate Change on Wildfire in
1415 California. *Earth's Future*, 7(8), 892-910. doi:<https://doi.org/10.1029/2019EF001210>

1416 [Williams, A.P. et al. \(2022\) Growing impact of wildfire on western US water supply. 119:e2114069119](https://doi.org/10.1073/pnas.2114069119)
1417 [doi:10.1073/pnas.2114069119](https://doi.org/10.1073/pnas.2114069119) %J *Proceedings of the National Academy of Sciences*

1418 Xia, Y., Mitchell, K., Ek, M., Cosgrove, B., Sheffield, J., Luo, L., . . . Lohmann, D. (2012). Continental-scale
1419 water and energy flux analysis and validation for North American Land Data Assimilation System
1420 project phase 2 (NLDAS-2): 2. Validation of model-simulated streamflow. *Journal of Geophysical*
1421 *Research: Atmospheres*, 117(D3). doi:<https://doi.org/10.1029/2011JD016051>

1422 [Yin D., Xue Z. G., Gochis D. J., Yu W., Morales M., & Rafieeinabab A. \(2020\) A Process-Based, Fully](https://doi.org/10.1029/2011JD016051)
1423 [Distributed Soil Erosion and Sediment Transport Model for WRF-Hydro 12:1840](https://doi.org/10.1029/2011JD016051)

1424 Zhang, J. et al. (2011). National Mosaic and Multi-Sensor QPE (NMQ) system: Description, results, and future
1425 plans. *Bull. Amer. Meteor. Soc.*, 92, 1321–1338, <https://doi.org/10.1175/2011BAMS-D-11-00047.1>.

1426 Zhang, J., ~~Y~~-Qi, ~~C~~-Y., Langston, ~~B~~C., Kaney, ~~K~~-B., & Howard, ~~K~~. (2014). A real-time algorithm for merging
1427 radar QPEs with rain gauge observations and orographic precipitation climatology. *J. Hydrometeor.*, 15,
1428 1794–1809, <https://doi.org/10.1175/JHM-D-13-0163.1>.

1429 Zhang, J. et al. (2016). Multi-Radar Multi-Sensor (MRMS) quantitative precipitation estimation: Initial
1430 operating capabilities. *Bull. Amer. Meteor. Soc.*, 97, 621–638, <https://doi.org/10.1175/BAMS-D-14-00174.1>.

1431 [Zhang S., Zhao, L., Delgado-Tellez, R., Bao, H. \(2018\) A physics-based probabilistic forecasting model for](https://doi.org/10.5194/nhess-18-969-2018)
1432 [rainfall-induced shallow landslides at regional scale Nat Hazards Earth Syst Sci 18:969-982](https://doi.org/10.5194/nhess-18-969-2018)
1433 [doi:10.5194/nhess-18-969-2018](https://doi.org/10.5194/nhess-18-969-2018)

Formatted: Font: 10.5 pt, Not Bold

Formatted: Left, Line spacing: single